

**NASA
Technical
Paper
2977**

1990

Modeling and Analysis of the Space Shuttle Nose-Gear Tire With Semianalytic Finite Elements

Kyun O. Kim and Ahmed K. Noor
*The George Washington University
Joint Institute for Advancement of Flight Sciences
Langley Research Center
Hampton, Virginia*

John A. Tanner
*Langley Research Center
Hampton, Virginia*



National Aeronautics and
Space Administration
Office of Management
Scientific and Technical
Information Division

Abstract

A computational procedure is presented for the geometrically nonlinear analysis of aircraft tires. The Space Shuttle orbiter nose-gear tire was modeled through use of a two-dimensional laminated anisotropic shell theory with the effects of variation in material and geometric parameters included. The four key elements of the procedure are (1) semi-analytic finite elements in which the shell variables are represented by Fourier series in the circumferential direction and piecewise polynomials in the meridional direction; (2) a mixed formulation with the fundamental unknowns consisting of strain parameters, stress-resultant parameters, and generalized displacements; (3) multilevel operator splitting to effect successive simplifications and to uncouple the equations associated with different Fourier harmonics; and (4) multilevel iterative procedures and reduction techniques to generate the response of the shell. Numerical results of the Space Shuttle orbiter nose-gear tire model are compared with experimental measurements of the tire subjected to inflation loading.

Introduction

Because of the axial symmetry of undeformed tires, it is desirable in their modeling and analysis to exploit the substantial capability that currently exists for the numerical analysis of shells of revolution. The most commonly used approach for the analysis of shells of revolution is based on the representation of the shell variables and loads by a Fourier series in the circumferential coordinate θ , combined with the use of a numerical discretization technique (such as finite elements, finite differences, or numerical integration) in the meridional direction. (See, for example, refs. 1 to 7.) Such an approach has the major advantages of accuracy and stability (i.e., no locking or spurious modes) over approaches which use two-dimensional shell elements. Moreover, for linear problems of shells with uniform circumferential properties, the Fourier series representation permits separation of variables and the equations uncouple in harmonics. However, when applied to the analysis of tires the approach has the following drawbacks, which can make the computational cost of the geometrically nonlinear analysis of tires quite expensive:

1. For geometrically nonlinear problems, the unknowns associated with different harmonics are coupled (see refs. 8 and 9).

2. Even for linear problems, because of the anisotropy of the cord-tire composites, the symmetric and antisymmetric responses (with respect to $\theta = 0$) associated with each harmonic are coupled.

3. For localized loading (e.g., contact pressure on the tire), a large number of harmonics are needed to accurately predict the response.

Research on tire modeling and analysis at NASA Langley Research Center has focused on developing accurate and cost-effective strategies for predicting tire response. Included in the research is the development of analysis procedures for substantial reduction of the computational expense resulting from the harmonic and anisotropic couplings (items 1 and 2) and the generation of the response associated with large numbers of harmonics (item 3). The present paper summarizes the status of these development activities. To demonstrate the capabilities of the analysis techniques, numerical studies were conducted with the Space Shuttle orbiter nose-gear tire. Numerical results are presented for an inflated Space Shuttle tire, and these results are compared with experimental measurements.

Notation

A_{ij}, B_{ij}, D_{ij}	stiffness coefficients of two-dimensional shell model of tire ($i, j = 1, 2, 6$)
b_1, b_2	parameters defining geometry of tire cross section (see fig. 3)
c_{ij}	stiffness coefficients of individual unidirectional plies ($i, j = 1, 2, 4, 5$, and 6)
d	diameter of tire nylon cord
$\{E\}$	vector of strain parameters for shell model of tire (see eq. (2))
E_c, E_r	Young's moduli for nylon cord and rubber
$\{E\}_n$	vector of strain parameters associated with n th Fourier harmonic for shell model of tire (see eq. (2) and table 1)
E_{T_o}	elastic modulus (see tables 7 and 8 and fig. 9)
E_1, E_2	elastic moduli in direction of tire cord and normal to it
epi	cord end count, ends per inch
f_c	volume fraction of nylon cord in individual plies of tire
$\{f\}^{(n)}$	vector defined in equations (5)
G_c, G_r	shear moduli for tire cord and rubber

$\{G\}^{(n)}$	vector of nonlinear terms associated with n th Fourier harmonic (see eqs. (5))	$N_s, N_\theta, N_{s\theta}$	extensional stress resultants (see fig. 1 and table 1)
G_{12}, G_{13}	shear moduli in plane of tire cord	\mathbf{n}	vector normal to reference surface of tire
G_{23}	shear modulus normal to plane of tire cord	n	Fourier harmonic (circumferential wave number)
$\{H\}$	vector of stress-resultant parameters for shell model of tire (see eq. (3))	n_o	Fourier harmonic at which global approximation vectors are generated
$\{H\}_n$	vectors of stress-resultant parameters associated with n th Fourier harmonic for shell model of tire (see eq. (3) and table 1)	$\{P\}, \{\hat{P}\}$	right-side vectors in equations (13)
h	total thickness of tire	$\{P\}^{(n)}$	consistent load vector associated with n th Fourier harmonic for tire (see eqs. (5))
\bar{h}	nondimensional thickness of tire (see fig. 2)	p_n	normal pressure components associated with n th Fourier harmonic for shell model of tire (see eq. (1))
h_k	thickness of individual layers of two-dimensional shell model	p_o	intensity of localized normal loading of tire (see fig. 10)
h_o	total thickness of tire at $\xi = 0$ (see fig. 3)	\bar{p}_o	inflation pressure acting normal to inner surface of tire (see figs. 3 and 4)
$[\tilde{K}], [\hat{K}]$	matrices defined in equations (6)	p_s, p_θ, p	intensity of external loading in coordinate directions (see fig. 1)
$[\bar{K}]^{(IJ)}$	matrix containing nonlinear terms (see eqs. (9) and (11))	Q_s, Q_θ	transverse-shear stress resultants (see fig. 1 and table 1)
$[K]^{(n)}$	linear matrix associated with n th Fourier harmonic (see eqs. (5))	$\{q\}, \{\hat{q}\}$	load vectors associated with reduced equations (see eqs. (18) and (19))
$[K_o], [K_a]$	submatrices of $[K]^{(n)}$ (see eqs. (8))	R_1, R_2	principal radii of curvature in meridional and circumferential directions of reference surface of shell model
$[\tilde{k}], [\hat{k}]$	matrices associated with reduced equations (see eqs. (16) and (17))	r	normal distance from tire axis to reference surface (see fig. 3)
l	number of segments along tire surfaces	r_o	$= r$ at $\xi = 0$
$M_s, M_\theta, M_{s\theta}$	bending and twisting stress resultants (see fig. 1 and table 1)	$[S_o], [S], [R]$	submatrices of $[K]^{(n)}$ (see eqs. (8))
m	number of displacement nodes in element	s	meridional coordinate of tire (see fig. 1); number of parameters used in approximating each stress resultant and strain components in element
N	number of Fourier harmonics which are greater than or equal to 1	s_i	polygonal arc lengths of segment of tire surfaces (see eq. (A2))
N^i	shape functions used in approximating generalized displacements and external loading		
\bar{N}^l	shape functions used in approximating stress resultants and strain components		

U	strain energy density of shell model of tire	$\kappa_{1,0}, \kappa_{2,0}$	principal curvatures at $\xi = 0$
u, v, w	displacement components of reference surface of tire in meridional, circumferential, and normal directions (see fig. 1 and table 1)	$\tilde{\lambda}$	tracing parameter identifying coupling between different Fourier harmonics (see eqs. (12))
$\{X\}$	vector of generalized nodal displacement coefficients for tire (see eq. (4))	ν_c, ν_r	Poisson's ratios of tire cord and rubber
$\{X\}_n$	vector of generalized nodal displacement coefficients associated with n th Fourier harmonic for shell model of tire (see table 1)	ν_{12}, ν_{21}	major and secondary Poisson's ratios in individual plies
\mathbf{x}	position vector for points to be interpolated along segment of tire surfaces (see eqs. (A1))	ξ	dimensionless coordinate along meridian (see fig. 2)
x, z	Cartesian coordinates (see fig. 3)	σ	tension factor
x_3	coordinate normal to tire reference surfaces (see fig. 1)	σ'	normalized tension factor (see eq. (A4))
\mathbf{y}_i	position vector for data points of segment (see eqs. (A1))	σ_1, σ_2	in-plane stress components in tire cord direction and normal to it
$\{Z\}_n$	vector of unknowns associated with n th Fourier harmonic (see eqs. (7))	$\tau_{12}, \tau_{13}, \tau_{23}$	shear stress components in principal material axes
β	contact angle in meridional direction (see fig. 10)	ϕ	angle between normal to meridian and x -axis (see fig. 3)
$[\Gamma]$	matrix of global approximation vectors (see eqs. (14))	ϕ_s, ϕ_θ	rotational components of reference surface of tire (see fig. 1 and table 1)
$\gamma_{12}, \gamma_{13}, \gamma_{23}$	shear strain components in principal material axis	$\{\Psi\}_n$	vector of amplitudes of global approximation vectors (see eqs. (14))
$\varepsilon_s, \varepsilon_\theta, 2\varepsilon_{s\theta}$	extensional strains of reference surface of tire	Superscripts:	
$2\varepsilon_{s3}, 2\varepsilon_{\theta3}$	transverse-shear strains of shell model of tire	i	index of shape functions for approximating generalized displacements and external loadings; ranges from 1 to m
$\varepsilon_1, \varepsilon_2$	in-plane strain components in tire cord direction and normal to it	l	index of shape functions for approximating stress resultants and strain components; ranges from 1 to s
θ	circumferential (hoop) coordinate of tire (see fig. 1)	r	number of iterational cycles
$\tilde{\theta}$	orientation angle used in equation (24) and table 6	t	matrix transposition
θ_k	orientation angle of tire cord, deg	–	coefficient of sine terms in Fourier series
$\kappa_s, \kappa_\theta, 2\kappa_{s\theta}$	bending strains of tire	Subscripts:	
κ_1, κ_2	principal curvatures in meridional and circumferential directions of reference surface of shell model	max	maximum value
		n	Fourier harmonic

Analysis

Mathematical Formulation

In the present study we model the Space Shuttle orbiter nose-gear tire using a moderate-rotation

Sanders-Budiansky shell theory with the effects of transverse shear deformation and laminated anisotropic material response included (refs. 10 and 11). A total Lagrangian formulation is used and the fundamental unknowns consist of the five generalized displacements, the eight stress resultants, and the corresponding eight strain components of the middle surface. The sign convention for the different tire stress resultants and generalized displacements is shown in figure 1. The concepts presented in the succeeding sections can be extended to higher order shear deformation theories as well as to three-dimensional continuum theory.

Spatial Discretization of the Tire

Each of the generalized displacements, the stress resultants, and the strain components is expanded in a Fourier series of the circumferential coordinate θ . The discretization in the meridional direction is performed through the use of a three-field mixed finite-element model. The following expressions are used for approximating the external loading, strain components, stress resultants, and generalized displacements within each element:

$$p(s, \theta) = N^i \left(\sum_{n=0}^{\infty} p_n^i \cos n\theta + \sum_{n=1}^{\infty} \bar{p}_n^i \sin n\theta \right) \quad (1)$$

$$E(s, \theta) = \bar{N}^l \left(\sum_{n=0}^{\infty} E_n^l \cos n\theta + \sum_{n=1}^{\infty} \bar{E}_n^l \sin n\theta \right) \quad (2)$$

$$H(s, \theta) = \bar{N}^l \left(\sum_{n=0}^{\infty} H_n^l \cos n\theta + \sum_{n=1}^{\infty} \bar{H}_n^l \sin n\theta \right) \quad (3)$$

$$X(s, \theta) = N^i \left(\sum_{n=0}^{\infty} X_n^i \cos n\theta + \sum_{n=1}^{\infty} \bar{X}_n^i \sin n\theta \right) \quad (4)$$

where N^i are the shape functions used in approximating the generalized displacements and external loading in the meridional direction; \bar{N}^l are the shape functions used in approximating the strain components and stress resultants; p_n^i and \bar{p}_n^i refer to the normal pressure coefficients; X_n^i and \bar{X}_n^i refer to the generalized displacement coefficients; E_n^l and \bar{E}_n^l refer to the strain parameters; H_n^l and \bar{H}_n^l refer to the stress-resultant parameters; and subscript n refers to

the quantities associated with the Fourier harmonic n . Note that the degree of the polynomial shape functions \bar{N}^l is lower than that of N^i . Moreover, the continuity of the strain components and stress resultants is not imposed at the interelement boundaries and, therefore, the strain and stress-resultant parameters can be eliminated on the element level.

In equations (1) to (4), the range of i is 1 to m , the number of displacement nodes in the element; the range of l is 1 to s , the number of parameters used in approximating each of the strain components and stress resultants. The shell variables without a bar are the coefficients of the cosine series, the shell variables with a bar are the coefficients of the sine series, and a repeated superscript denotes summation over its entire range. Henceforth, the vectors of the 10 generalized displacement parameters, of the 16 strain parameters, and of the 16 stress-resultant parameters chosen in association with the harmonic n are denoted by $\{X\}_n$, $\{H\}_n$, and $\{E\}_n$, respectively. These vectors can be decomposed into symmetric and antisymmetric sets (with respect to $\theta = 0$) as shown in table 1.

Governing Equations

The governing discrete equations of the tire are obtained through application of the three-field Hu-Washizu mixed variational principle (see ref. 12). If the number of terms (harmonics) retained in the Fourier series is $N + 1$, then the governing equations can be written in the following compact form:

$$\begin{Bmatrix} f^{(0)} \\ f^{(1)} \\ \vdots \\ f^{(N)} \end{Bmatrix} = \begin{bmatrix} K^{(0)} & & & \\ & K^{(1)} & & \\ & & \ddots & \\ & & & K^{(N)} \end{bmatrix} \begin{Bmatrix} Z_0 \\ Z_1 \\ \vdots \\ Z_N \end{Bmatrix} + \begin{Bmatrix} G^{(0)}(Z_0, Z_1, \dots, Z_N) \\ G^{(1)}(Z_0, Z_1, \dots, Z_N) \\ \vdots \\ G^{(N)}(Z_0, Z_1, \dots, Z_N) \end{Bmatrix} - \begin{Bmatrix} P^{(0)} \\ P^{(1)} \\ \vdots \\ P^{(N)} \end{Bmatrix} = 0 \quad (5)$$

where $\{Z\}_n$ ($n = 0, 1, \dots, N$) is the vector of unknowns associated with the n th harmonic and includes vectors of strain parameters $\{E\}_n$, of stress-resultant parameters $\{H\}_n$, and of generalized

displacements $\{X\}_n$; $[K]^{(n)}$ is a linear matrix; $\{G\}^{(n)}$ is a vector of nonlinear terms; and $\{P\}^{(n)}$ is a consistent load vector.

The following observations can be made about the governing equations (eqs. (5)):

1. The first matrix on the left side of equations (5) is block diagonal, which is a direct consequence of the orthogonality of the trigonometric functions. The orthogonality of trigonometric functions leads to uncoupling of the equations associated with the different Fourier harmonics for the linear case. For the nonlinear case, the vector $\{G\}^{(n)}$ couples the unknowns associated with *all* the harmonics. (See, for example, ref. 9.)
2. The contributions of the different Fourier harmonics and the anisotropic (nonorthotropic) material coefficients to the governing equations can be identified as follows:
 - a. *Fourier harmonics*—The block-diagonal matrix $[K]^{(n)}$ ($n \geq 1$) in equations (5) is linear in the Fourier harmonic n . Therefore, $[K]^{(n)}$ can be expressed as the sum of two matrices as follows:

$$[K]^{(n)} = [\tilde{K}] + n[\hat{K}] \quad (6)$$

where both $[\tilde{K}]$ and $[\hat{K}]$ are independent of n . The nonlinear vector $\{G\}^{(n)}$ is quadratic in n .

- b. *Anisotropy (nonorthotropy)*—A unique feature of the mixed formulation used herein is that the anisotropic (nonorthotropic) material coefficients are included only in the linear matrix $[K]^{(n)}$. For the linear case, these anisotropic coefficients result in the coupling

between the symmetric and antisymmetric shell parameters (see ref. 13 and table 2).

3. If the vector $\{Z\}_n$ is partitioned into subvectors of parameters of strains, stress resultants, and generalized displacements, that is,

$$\{Z\}_n = \begin{Bmatrix} E \\ H \\ X \end{Bmatrix}_n \quad (7)$$

then the matrix $[K]^{(n)}$ can be written in the following form:

$$[K]^{(n)} = \begin{bmatrix} K_o + K_a & -R & \cdot \\ -R^t & \cdot & S_o + nS \\ \cdot & S_o^t + nS^t & \cdot \end{bmatrix} \quad (8)$$

where the submatrices $[K_o]$ and $[K_a]$ contain the contributions of the orthotropic and anisotropic (nonorthotropic) material coefficients. The explicit forms of the submatrices $[K_o]$, $[K_a]$, $[S_o]$, $[S]$, and $[R]$ are given in references 14 and 15.

4. The nonlinear vector $\{G\}^{(n)}$ contains bilinear terms in $\{H\}_n$ and $\{X\}_n$ as well as quadratic terms in $\{X\}_n$.

Generation of the Nonlinear Response of the Tire

For a given external loading, the governing nonlinear equations (eqs. (5)) are solved by using the Newton-Raphson iterative technique. The recursion formulas for the r th iterational cycle are

$$\left(\begin{bmatrix} K^{(0)} & & \\ & K^{(1)} & \\ & & \ddots \\ & & & K^{(N)} \end{bmatrix} + \begin{bmatrix} \bar{K}^{(00)} & \bar{K}^{(01)} & \dots & \bar{K}^{(0N)} \\ & 0 & \dots & \bar{K}^{(1N)} \\ & & \ddots & \vdots \\ & & & 0 \end{bmatrix} \right)^{(r)} \begin{Bmatrix} \Delta Z_0 \\ \Delta Z_1 \\ \vdots \\ \Delta Z_N \end{Bmatrix}^{(r)} = - \begin{Bmatrix} f^{(0)} \\ f^{(1)} \\ \vdots \\ f^{(N)} \end{Bmatrix}^{(r)} \quad (9)$$

and

$$\begin{Bmatrix} Z_0 \\ Z_1 \\ \vdots \\ Z_N \end{Bmatrix}^{(r+1)} = \begin{Bmatrix} Z_0 \\ Z_1 \\ \vdots \\ Z_N \end{Bmatrix}^{(r)} + \begin{Bmatrix} \Delta Z_0 \\ \Delta Z_1 \\ \vdots \\ \Delta Z_N \end{Bmatrix}^{(r)} \quad (10)$$

where

$$[\bar{K}]^{(IJ)} = \frac{\partial}{\partial Z_J} \{G\}^{(I)} \quad (I, J = 1 \text{ to } N) \quad (11)$$

For each Newton-Raphson iteration (represented by eqs. (9) and (10)), another iteration loop is performed using the preconditioned conjugate gradient (PCG) technique to account for the coupling between the different harmonics (i.e., the submatrix $[\bar{K}]^{(IJ)}$). In the inner iteration loop the following uncoupled equations are solved:

$$\left. \begin{aligned} ([K]^{(0)} + [\bar{K}]^{(00)(r)}) \{\Delta Z\}_0^{(r)} &= -\{f\}^{(0)(r)} - \check{\lambda} \left([\bar{K}]^{(01)} \{\Delta Z\}_1 \right. \\ &\quad \left. + [\bar{K}]^{(02)} \{\Delta Z\}_2 + \dots + [\bar{K}]^{(0N)} \{\Delta Z\}_N \right)^{(r)} \\ [K]^{(1)} \{\Delta Z\}_1^{(r)} &= -\{f\}^{(1)(r)} - \check{\lambda} \left([\bar{K}]^{(10)} \{\Delta Z\}_0 + [\bar{K}]^{(12)} \{\Delta Z\}_2 \right. \\ &\quad \left. + \dots + [\bar{K}]^{(1N)} \{\Delta Z\}_N \right)^{(r)} \\ &\vdots \\ [K]^{(N)} \{\Delta Z\}_N^{(r)} &= -\{f\}^{(N)(r)} - \check{\lambda} \left([\bar{K}]^{(N0)} \{\Delta Z\}_0 + [\bar{K}]^{(N1)} \{\Delta Z\}_1 + \dots \right)^{(r)} \end{aligned} \right\} \quad (12)$$

where $\check{\lambda}$ is a tracing parameter which identifies the coupling between the different Fourier harmonics. When $\check{\lambda} = 1$ equations (12) are equivalent to equations (9), and when $\check{\lambda} = 0$ the equations uncouple in harmonics. Note that because of the special structure of the Jacobian matrix in equations (9), only the left side associated with the zeroth harmonic needs to be updated in each iteration. An efficient technique is described in the next subsection for solving equations (12).

Efficient Generation of the Response Associated With Different Harmonics

An efficient procedure is presented herein for generating the tire responses associated with different harmonics (solution of eqs. (12)). The basic idea of this procedure is to approximate the tire response associated with the range of Fourier harmonics, $1 \leq n \leq N$, by a linear combination of a few global approximation vectors that are generated at a particular value of the Fourier harmonic within that range. The full equations of the finite-element model are solved for only a single Fourier harmonic, and the responses corresponding to the other Fourier harmonics are generated using a reduced system of equations with considerably fewer degrees of freedom. The proposed procedure can be conveniently divided into two phases: (1) restructuring equations (12), for $1 \leq n \leq N$, to delineate the dependence on the Fourier harmonic n , and (2) generating global ap-

proximation vectors (or modes) to approximate the response associated with a range of values of the Fourier harmonic and determining the amplitudes of the modes. Application of the procedure to stress and vibration problems of anisotropic shells of revolution is described in references 16 and 17. Its application to the solution of equations (12) is outlined subsequently.

Restructuring of the governing equations.

If equations (6) and (8) are used, the governing equations for the harmonic n ($1 \leq n \leq N$) can be embedded in a single-parameter family of equations and written in the following compact form:

$$([\tilde{K}] + n[\hat{K}]) \{\Delta Z\}_n = \{P(n)\} + \check{\lambda} \{\hat{P}(n)\} \quad (13)$$

The two vectors $\{P(n)\}$ and $\{\hat{P}(n)\}$ are quadratic in n .

Basis reduction and reduced system of equations. The basis reduction is achieved by approximating the vector $\{\Delta Z\}_n$, for a certain range of Fourier harmonics, $1 \leq n \leq N$, by a linear combination of a few global approximation vectors which are generated at a particular value of the Fourier harmonic within that range. The approximation is expressed by the following transformation:

$$\{\Delta Z\}_n = [\Gamma] \{\Psi\}_n \quad (14)$$

where $[\Gamma]$ is a transformation matrix whose columns are the preselected approximation vectors, and $\{\Psi\}_n$ is a vector of unknown parameters representing the amplitudes of the global approximation vectors for the harmonics n . The number of components of $\{\Psi\}_n$ is much less than the number of components of $\{\Delta Z\}_n$.

A Bubnov-Galerkin technique is now used to replace the original equations (eqs. (13)) by the following reduced equations in $\{\Psi\}_n$:

$$([\tilde{k}] + n[\hat{k}]) \{\Psi\}_n = \{q\} + \check{\lambda}\{\hat{q}\} \quad (15)$$

where

$$[\tilde{k}] = [\Gamma]^t [\tilde{K}] [\Gamma] \quad (16)$$

$$[\hat{k}] = [\Gamma]^t [\hat{K}] [\Gamma] \quad (17)$$

$$\{q\} = [\Gamma]^t \{P(n)\} \quad (18)$$

$$\{\hat{q}\} = [\Gamma]^t \{\hat{P}(n)\} \quad (19)$$

Selection and generation of global approximation vectors. The global approximation vectors are selected to be the response associated with a single Fourier harmonic n_o and its various-order derivatives with respect to n . Henceforth, the derivatives of the response with respect to n are referred to as "path derivatives." The matrix $[\Gamma]$ in equations (14) is therefore given by

$$[\Gamma] = \left[\begin{array}{cccc} \{\Delta Z\} & \frac{\partial}{\partial n} \{\Delta Z\} & \frac{\partial^2}{\partial n^2} \{\Delta Z\} & \cdots \end{array} \right]_{n_o} \quad (20)$$

The path derivatives are obtained by successive differentiation of the governing equations (eqs. (13)). The recursion relations for the first three global approximation vectors can be written in the following form:

$$([\tilde{K}] + n_o[\hat{K}]) \{\Delta Z\}_{n_o} = \{P\} + \check{\lambda}\{\hat{P}\} \quad (21)$$

$$\begin{aligned} ([\tilde{K}] + n_o[\hat{K}]) \frac{\partial}{\partial n} \{\Delta Z\}_{n_o} &= \frac{\partial}{\partial n} \{P\} + \check{\lambda} \frac{\partial}{\partial n} \{\hat{P}\} \\ &\quad - [\hat{K}] \{\Delta Z\}_{n_o} \end{aligned} \quad (22)$$

$$\begin{aligned} ([\tilde{K}] + n_o[\hat{K}]) \frac{\partial^2}{\partial n^2} \{\Delta Z\}_{n_o} &= \frac{\partial^2}{\partial n^2} \{P\} + \check{\lambda} \frac{\partial^2}{\partial n^2} \{\hat{P}\} \\ &\quad - 2[\hat{K}] \frac{\partial}{\partial n} \{\Delta Z\}_{n_o} \end{aligned} \quad (23)$$

Note that the left-side matrix in equations (21) to (23) is the same, and therefore it needs to be decomposed only once in the process of generating all the global approximation vectors.

Comments on proposed procedure. The following comments are made concerning the foregoing procedure for generating the responses associated with different harmonics:

1. The particular choice of the global approximation vectors used herein provides a direct quantitative measure of the sensitivity of the different response quantities of the tire to the circumferential wave number (the Fourier harmonic) n .
2. For problems requiring large numbers of Fourier harmonics (e.g., 100 or more), the range of n is divided into intervals of fewer (e.g., 7) harmonics each; the global approximation vectors and reduced equations are generated at an intermediate value of n within each interval, and the responses associated with the values of n within that interval are generated by the foregoing procedure. Note that higher accuracy of the reduced solutions can be obtained by marching backward as well as forward in the n -space with the reduced equations.
3. The foregoing procedure can be directly applied to the solution of the governing nonlinear equations (eqs. (5)). This is accomplished by using a reduction method, with the control parameter selected to be load, displacement, or arc length in the solution space and the global approximation vectors selected to be the various-order derivatives of the response quantities with respect to the control parameter (see ref. 14). The global approximation vectors are obtained by successive differentiation of the governing equations (eqs. (5)) with respect to the control parameter. The left-side matrix of those equations has the same form as that of equations (9). If the global approximation vectors are evaluated at zero value for the control parameter, the matrix $[\bar{K}]^{(IJ)}$ on the left side of equations (9) vanishes and the equations uncouple in harmonics. The application of the foregoing procedure considerably reduces the computational effort in generating the global approximation vectors and greatly enhances the effectiveness of the reduction method.
4. The computational effort can be further reduced by using the procedure outlined in reference 14 to uncouple the equations associated with the symmetric and antisymmetric shell parameters (with respect to $\theta = 0$). The procedure is based on transferring the anisotropic (nonorthotropic)

terms (submatrix $[K_a]$ in eqs. (8)) to the right sides of equations (12) and adding another level of PCG iterations to account for them.

Results and Discussion

Numerical studies were performed to assess the accuracy of the two-dimensional shell model tire and the effectiveness of the computational procedure described in the preceding section, for generating the response associated with different harmonics. Herein, the application of the model and the computational procedure to the Space Shuttle orbiter nose-gear tire are presented. The geometric and material characteristics of the tire are given in figures 2 and 3. The Space Shuttle orbiter nose-gear tire is a 32×8.8 type VII bias-ply tire with a ply rating of 16. The tire carcass is constructed of 10 lamina of nylon and rubber with an additional reinforcing ply beneath the tire tread as shown in figure 2. The tire has a three-groove tread, but the model assumes a smooth tread instead. The rated load for the tire is 15 000 lb at an inflation pressure of 320 psi.

The numerical studies were performed with three-field mixed finite-element models used for the discretization of the tire in the meridional direction. Linear interpolation functions were used to approximate each of the stress resultants and strain components, and quadratic Lagrangian interpolation functions were used to approximate each of the generalized displacements. The integrals in the governing equations were evaluated with a two-point Gauss-Legendre numerical quadrature formula. Because of the symmetry of the shell meridian and loading, only half of the tire meridian was analyzed. The finite-element models used are shown in figure 4.

Modeling of the Tire Geometry

The Space Shuttle orbiter nose-gear tire was modeled as a two-dimensional laminated shell with variable thickness and variable stiffness. The outer surface of the tire was taken to be the reference surface of the shell model. A tire was cut into sections and used to obtain accurate measurements for the cross-sectional shape of the uninflated tire. A smoothed spline under tension was used to fit a curve through the measured coordinates of the cross-sectional profile in a least-squares sense (see refs. 18 and 19). Because of symmetry, only half of the cross section was modeled. A smooth variation of the second derivative, $\frac{d^2x}{dz^2}$, was achieved by adjusting the standard deviations of the measured profile at the data points. For a detailed description of spline smoothing techniques, see references 19 to 21.

The spline function, with the tension factor set equal to 0.1 and slope continuity enforced at both ends of the curves, was used to generate additional points along the tire meridian. The interpolation procedure is outlined in appendix A and the resulting geometric characteristics of the tire are presented in appendix B and figure 5. The thickness of the tire carcass at the nodal points of the finite-element model was computed along the normal vector to the tire reference (outer) surface by locating the points of intersection of the normal vectors with the inner surface of the tire carcass. To facilitate these computations the tire inner surface was approximated by a set of third-degree polynomials.

Evaluation of Stiffness Coefficients of the Two-Dimensional Shell Model

The cord-rubber composite was treated as a laminated material. For the purpose of computing stiffness variations in the meridional direction, the tire model was divided into seven regions, as shown in figure 2. Thicknesses of the individual carcass plies were measured at the interfaces between the regions and are given in table 3. A linear variation was assumed for the thickness within each region. The thickness of the tire tread and sidewall covering was computed by subtracting the sum of the individual ply thicknesses from the total thickness of the carcass at each location.

The material properties of the different plies were obtained with the mechanics of material approach, which has been widely applied to rigid composites. (See refs. 22 and 23.) The elastic constants of the tire constituents used in this study are presented in table 4. It was assumed that nylon cords of two different diameters were used in the construction of the tire: $d = 0.022$ in. for the bottom two plies and the tread reinforcement in region I, and $d = 0.031$ in. for all other plies.

The cord end counts (epi) for individual plies at the region interfaces are given in table 5. A linear variation was assumed for epi within each region. The formulas for evaluating the composite elastic coefficients for each ply, from the properties of the ply constituents, are given in appendix C.

The stress-strain relations of the two-dimensional shell were obtained by first transforming the stiffnesses of each of the individual layers to the global shell coordinates (s and θ) and then integrating these coefficients through the thickness. The cord orientations in the individual plies of each region are given in table 6. The following formula was used to determine

θ_k , the angle (in degrees) measured from the s -axis to the θ -axis, at the numerical quadrature points:

$$\bar{\theta} = \text{Max} \left\{ \left(54.382 - 3.884\xi - 148.96\xi^2 \right)^\circ, 33^\circ \right\} \quad (24)$$

where ξ is the dimensionless coordinate along the tire meridian.

The resulting shell constitutive relations are given in appendix C. The meridional variations of the stiffness coefficients of the shell model are shown in figure 6.

Case of Inflation Pressure

To assess the accuracy of the shell model of the tire, the deformations produced by uniform inflation pressure of $\bar{p}_o = 320$ psi, acting normal to the inner surface, were calculated using the geometrically nonlinear shell theory. Twelve finite elements were used in modeling half the cross section (a total of 384 strain parameters, 384 stress-resultant parameters, and 243 nonzero generalized displacements; see fig. 4(a)). The calculated values were compared with the experimental data obtained on the Space Shuttle orbiter nose-gear tire. (See fig. 2.) The results are summarized in figures 7 to 9. Close agreement between the predicted deformations and experimental results is demonstrated in figure 7. Figures 8 and 9 show the meridional variations of the generalized displacements, stress resultants, and strain energy densities. As shown in figure 9 for the case of inflation pressure, the transverse-shear strain energy density is considerably smaller than the extensional and bending strain energy density.

Case of Localized Loading

To assess the effectiveness of the computational procedure, linear solutions were obtained for a localized normal loading on the outer surface simulating contact pressure. The normal loading (in pounds per square inch) is given by the following equations, which model experimental data obtained at Langley on the shuttle tire:

$$p = \begin{cases} -\frac{p_o\beta}{\pi} - \sum_{n=1}^{10} p_n \cos n\theta & (-0.2 < \xi < 0.2) \\ 0 & (|\xi| > 0.2) \end{cases} \quad (25)$$

where

$$p_n = \frac{2p_o}{n\pi} \sin n\beta \quad (26)$$

and p_o and β are functions of ξ as shown in figure 10.

Because of the symmetry of the shell meridian and loading, only half the meridian is analyzed using 37 elements (a total of 1184 stress-resultant parameters, 1184 strain parameters, and 743 nonzero displacement degrees of freedom; see fig. 4(b)). The boundary conditions at the centerline are taken to be the symmetric or antisymmetric conditions. Typical results are presented in figures 11 and 12 and in tables 7 and 8.

The foregoing procedure was applied to this problem, and 10 global approximation vectors were evaluated at $n_o = 5$ and used to generate the tire response for $n = 1$ to 10. Accuracy of the generalized displacements obtained by the procedure with 8, 10, and 15 global approximation vectors is indicated in figures 11 and 12. Each generalized displacement in figures 11 and 12 is normalized by dividing by its maximum absolute value given in tables 7 and 8. Generalized displacements predicted by the foregoing procedure with 15 vectors are almost indistinguishable from those predicted by the direct finite-element solution.

Conclusions

A computational procedure is presented for the geometrically nonlinear analysis of aircraft tires. The Space Shuttle orbiter nose-gear tire was modeled through use of a two-dimensional laminated anisotropic shell theory with the effects of variation in material and geometric parameters included.

The governing discrete equations of the tire are obtained through application of the three-field Hu-Washizu mixed variational principle. The multilevel operator splitting is used to (1) uncouple the equations associated with different harmonics, (2) identify the effects of different Fourier harmonics, and (3) delineate the effect of anisotropic (nonorthotropic) material properties. The nonlinear governing finite-element equations of the tire are solved with the Newton-Raphson iterative procedure. An efficient procedure is presented for the solution of the resulting algebraic equations at each iteration, associated with different Fourier harmonics. The effectiveness of this procedure is demonstrated by means of a numerical example of the linear response of the Space Shuttle orbiter nose-gear tire subjected to inflation loading. The tire model is subjected to localized normal loading on the outer surface (simulating the contact pressure).

Results of the present study suggest the following conclusions relative to the two-dimensional shell model used in simulating the response of the tire and to the proposed computational procedure for generating the tire response associated with different Fourier harmonics:

1. A two-dimensional shell model with variable geometric and stiffness characteristics accurately predicts the deformation of the tire when subjected to inflation pressure.
2. Use of path derivatives (derivatives of the response with respect to the Fourier harmonic) as global approximation vectors leads to accurate solutions with a small number of vectors. Therefore, the time required to solve the reduced equations is relatively small and the total time required to generate the response for a range of 10 Fourier harmonics is little more than that required for a *single* Fourier harmonic.
3. Global approximation vectors provide a direct measure of the sensitivity of the different response quantities to the circumferential wave (harmonic) number. Sensitivity of the global response can also be assessed with these vectors.
4. The reduction method used in the proposed computational procedure exploits the best elements of the finite-element method and of the Bubnov-Galerkin technique, as follows:
 - a. The finite-element method is used as a general approach for generating global approximation vectors. The full finite-element equations are solved only for a single Fourier harmonic.
 - b. The Bubnov-Galerkin technique is used as an efficient procedure for minimizing and distributing the error throughout the structure.
5. The reduction method extends the range of applicability of the Taylor series expansion by relaxing the requirement of using small changes in the circumferential wave number.

NASA Langley Research Center
 Hampton, VA 23665-5225
 January 22, 1990

Appendix A

Summary of the Equations for a Spline Under Tension

This appendix presents the interpolation procedure which uses a smoothed spline under tension to fit a curve through the measured coordinates of the cross-sectional profile in a least-squares sense. The cubic spline function requires that the second derivative be piecewise linear and continuous. Thus, the second derivative with the effect of tension is specified by

$$\ddot{\mathbf{x}}(s) - \sigma^2 \mathbf{x}(s) = \left[\ddot{\mathbf{x}}(s_i) - \sigma^2 \mathbf{y}_i \right] \frac{s_{i+1} - s}{s_{i+1} - s_i} + \left[\ddot{\mathbf{x}}(s_{i+1}) - \sigma^2 \mathbf{y}_{i+1} \right] \times \frac{s - s_i}{s_{i+1} - s_i} \quad (s_i \leq s \leq s_{i+1}) \quad (\text{A1})$$

where $\mathbf{x} = [x(s), z(s)]$ is the position vector for points along the segment; $\mathbf{y}_i = [x, z]_i$ is the corresponding data at point i ; a dot over a symbol refers to a derivative with respect to s . The chordal length (polygonal arc length) s_i is given by

$$\left. \begin{aligned} s_1 &= 0 \\ \text{and} \\ s_i &= s_{i-1} + [(x_i - x_{i-1})^2 + (z_i - z_{i-1})^2]^{1/2} \end{aligned} \right\} \quad (\text{A2})$$

After solving equations (A1) for $\mathbf{x}(s)$ and replacing $\mathbf{x}(s_i)$ with \mathbf{y}_i , we obtain

$$\begin{aligned} \mathbf{x}(s) = & \frac{\left[\ddot{\mathbf{x}}(s_i) / \sigma^2 \right] \sinh \sigma(s_{i+1} - s)}{\sinh \sigma(s_{i+1} - s_i)} \\ & + \frac{\left[\mathbf{y}_i - \ddot{\mathbf{x}}(s_i) / \sigma^2 \right] (s_{i+1} - s)}{s_{i+1} - s_i} \\ & + \frac{\left[\mathbf{x}(s_{i+1}) / \sigma^2 \right] \sinh \sigma(s - s_i)}{\sinh \sigma(s_{i+1} - s_i)} \\ & + \frac{\left[\mathbf{y}_{i+1} - \ddot{\mathbf{x}}(s_{i+1}) / \sigma^2 \right] (s - s_i)}{s_{i+1} - s_i} \quad (\text{A3}) \end{aligned}$$

From differentiating equations (A3) and equating right- and left-side derivatives at s_i (for $i = 2, 3, \dots, l-1$), we obtain a set of linear algebraic equations for $\ddot{\mathbf{x}}(s_i)$. With the assumption of a nonperiodic spline in which both slopes at s_1 and s_l are provided, the tridiagonal differential equation is easily solved.

Once the second derivatives at point $i = 1, 2, \dots, l$ are obtained, the first and second derivatives $\dot{\mathbf{x}}(s)$ and $\ddot{\mathbf{x}}(s)$ at the interpolated points are evaluated by differentiating equations (A3) and they are used to compute the geometric parameters of the tire in appendix B.

A normalized tension factor is used to eliminate a nonlinear behavior by setting (see ref. 24)

$$\sigma' = \frac{\sigma(s_l - s_1)}{l - 1} \quad (\text{A4})$$

In practice, if this factor is less than 0.001, the resulting curve is approximately a cubic spline, and if it is greater than 50, the curve is nearly piecewise linear. Note that s in equations (A1) to (A4) is not the actual arc length but the chordal length. Thus, the more data points one has from smoothing, the more accurate the arc length.

Appendix B

Geometric Characteristics of the Tire

This appendix presents the geometric characteristics derived from the application of the interpolation procedure described in appendix A. From this spline interpolation, we obtain the following information about the curve at each interpolated data point: s , x , z , $\frac{dx}{ds}$, $\frac{dz}{ds}$, $\frac{d^2x}{ds^2}$, and $\frac{d^2z}{ds^2}$. The geometric parameters of the tire are then evaluated as follows:

Normal vector:

$$\mathbf{n} = \begin{Bmatrix} \sin \phi \\ \cos \phi \end{Bmatrix} = \begin{Bmatrix} -\frac{dx/ds}{\sqrt{(dx/ds)^2 + (dz/ds)^2}} \\ \frac{dz/ds}{\sqrt{(dx/ds)^2 + (dz/ds)^2}} \end{Bmatrix}$$

Curvatures:

$$\kappa_1 = \frac{1}{R_1} = -\cos^3 \phi \left(\frac{d^2x}{dz^2} \right)$$

$$\kappa_2 = \frac{1}{R_2} = \frac{\cos \phi}{x}$$

Note that $x = r$, the normal distance from the axis to the reference surface, and $\frac{dx}{ds} = \frac{dr}{ds}$. Also note that the normal vector is used to compute the thickness, the components of the inflation pressure acting on the inner surface of the tire, and the transformation matrix with respect to the global coordinate system, if necessary.

Appendix C

Constitutive Relations for the Two-Dimensional Laminated Shell Model

This appendix presents the formulas for evaluating the composite elastic coefficients for each ply (from the properties of the ply constituents) and the resulting shell constitutive relations. The stress-strain relations of the orthotropic and unidirectional layers are given by

$$\begin{Bmatrix} \sigma_1 \\ \sigma_2 \\ \tau_{23} \\ \tau_{13} \\ \tau_{12} \end{Bmatrix} = \begin{bmatrix} c_{11} & c_{12} & \cdot & \cdot & \cdot \\ c_{12} & c_{22} & \cdot & \cdot & \cdot \\ \cdot & \cdot & c_{44} & \cdot & \cdot \\ \cdot & \cdot & \cdot & c_{55} & \cdot \\ \cdot & \cdot & \cdot & \cdot & c_{66} \end{bmatrix} \begin{Bmatrix} \varepsilon_1 \\ \varepsilon_2 \\ \gamma_{23} \\ \gamma_{13} \\ \gamma_{12} \end{Bmatrix}$$

where the reduced stiffnesses c_{ij} are given by

$$\begin{aligned} c_{11} &= \frac{E_1}{1 - \nu_{12}\nu_{21}} & c_{44} &= G_{23} \\ c_{12} &= \frac{E_1\nu_{21}}{1 - \nu_{12}\nu_{21}} & c_{55} &= G_{13} \\ c_{22} &= \frac{E_2}{1 - \nu_{12}\nu_{21}} & c_{66} &= G_{12} \end{aligned}$$

The elastic constants are computed by (see ref. 22)

$$\begin{aligned} E_1 &= E_c f_c + E_r (1 - f_c) \\ \nu_{12} &= \nu_c f_c + \nu_r (1 - f_c) \\ E_2 &= \frac{E_r [E_c (1 + 2f_c) + E_r (1 - f_c)]}{E_c (1 - f_c) + 2E_r (1 + 0.5f_c)} \\ G_{12} = G_{13} &= \frac{G_r [G_c + G_r + (G_c - G_r)f_c]}{[G_c + G_r - (G_c - G_r)f_c]} \\ G_{23} &= 0.6G_{12} \\ \nu_{21} &= \frac{\nu_{12}E_2}{E_1} \end{aligned}$$

where subscripts c and r represent the quantities of the nylon cord and the rubber, respectively, and f_c is the volume fraction of the nylon cord:

$$f_c = \frac{\pi d^2 (\text{epi})}{4h_k}$$

where d is cord diameter, h_k is the layer thickness, and epi is the cord end count (in ends per inch).

The relationships between the stress resultants and strain measures of the tire are given by

$$\begin{Bmatrix} N_s \\ N_\theta \\ N_{s\theta} \\ \text{---} \\ M_s \\ M_\theta \\ M_{s\theta} \\ \text{---} \\ Q_s \\ Q_\theta \end{Bmatrix} = \begin{bmatrix} A_{11} & A_{12} & \textcircled{A_{16}} & B_{11} & B_{12} & \textcircled{B_{16}} & \cdot & \cdot \\ & A_{22} & \textcircled{A_{26}} & B_{12} & B_{22} & \textcircled{B_{26}} & \cdot & \cdot \\ & & A_{66} & \textcircled{B_{16}} & \textcircled{B_{26}} & B_{66} & \cdot & \cdot \\ \text{---} & & & D_{11} & D_{12} & \textcircled{D_{16}} & \cdot & \cdot \\ & & & & D_{22} & \textcircled{D_{26}} & \cdot & \cdot \\ & \text{Symmetric} & & & & D_{66} & \cdot & \cdot \\ \text{---} & & & & & & A_{55} & \textcircled{A_{54}} \\ & & & & & & & A_{44} \end{bmatrix} \begin{Bmatrix} \varepsilon_s \\ \varepsilon_\theta \\ 2\varepsilon_{s\theta} \\ \text{---} \\ \kappa_s \\ \kappa_\theta \\ 2\kappa_{s\theta} \\ \text{---} \\ 2\varepsilon_{s3} \\ 2\varepsilon_{\theta3} \end{Bmatrix}$$

where A_{ij} , B_{ij} , and D_{ij} ($i, j = 1, 2, 6$) are shell stiffness coefficients. The nonorthotropic (anisotropic) terms are circled and dots indicate zero terms.

References

1. Bushnell, David: Analysis of Buckling and Vibration of Ring-Stiffened, Segmented Shells of Revolution. *Int. J. Solid Struct.*, vol. 6, no. 1, Jan. 1970, pp. 157-181.
2. Cohen, Gerald A.: FASOR - A Second Generation Shell of Revolution Code. *Comput. & Struct.*, vol. 10, nos. 1-2, Apr. 1979, pp. 301-309.
3. Goldberg, John E.: Computer Analysis of Shells. *Proceedings Symposium on the Theory of Shells To Honor Lloyd Hamilton Donnell*, D. Muster, ed., Univ. of Houston, 1967, pp. 3-22.
4. Grigorenko, Ya. M.: *Isotropic and Anisotropic Layered Shells of Revolution of Variable Stiffness*. Izdatel'stvo Naukova Dumka (Kiev, Russia), 1973.
5. Noor, Ahmed K.; and Stephens, Wendell B.: *Comparison of Finite-Difference Schemes for Analysis of Shells of Revolution*. NASA TN D-7337, 1973.
6. Padovan, Joseph; and Lestangi, Joseph F.: Complex Numerical Integration Procedure for Static Loading of Anisotropic Shells of Revolution. *Comput. & Struct.*, vol. 4, no. 6, Dec. 1974, pp. 1159-1172.
7. Sen, Subir K.; and Gould, Phillip L.: Free Vibration of Shells of Revolution Using FEM. *J. Eng. Mech. Div., American Soc. Civ. Eng.*, vol. 100, no. EM2, Apr. 1974, pp. 283-303.
8. Schaeffer, Harry G.; and Ball, Robert E.: Nonlinear Deflections of Asymmetrically Loaded Shells of Revolution. AIAA Paper No. 68-292, Apr. 1968.
9. Wunderlich, W.; Cramer, H.; and Obrecht, H.: Application of Ring Elements in the Nonlinear Analysis of Shells of Revolution Under Nonaxisymmetric Loading. *Comput. Methods Appl. Mech. & Eng.*, vol. 51, no. 1-3, Sept. 1985, pp. 259-275.
10. Budiansky, Bernard: Notes on Nonlinear Shell Theory. *J. Appl. Mech.*, vol. 35, no. 2, June 1968, pp. 393-401.
11. Sanders, J. Lyell, Jr.: Nonlinear Theories for Thin Shells. *Q. Appl. Math.*, vol. 21, no. 1, Apr. 1963, pp. 21-36.
12. Washizu, Kyuichiro: *Variational Methods in Elasticity and Plasticity*. Third ed. Pergamon Press Inc., c.1982.
13. Noor, Ahmed K.; and Peters, Jeanne M.: Analysis of Laminated Anisotropic Shells of Revolution. *J. Eng. Mech. Div., American Soc. Civ. Eng.*, vol. 113, no. 1, Jan. 1987, pp. 49-65.
14. Noor, Ahmed K.; Andersen, Carl M.; and Tanner, John A.: *Exploiting Symmetries in the Modeling and Analysis of Tires*. NASA TP-2649, 1987.
15. Noor, Ahmed K.; and Peters, Jeanne M.: Vibration Analysis of Laminated Anisotropic Shells of Revolution. *Comput. Methods Appl. Mech. & Eng.*, vol. 61, no. 3, Apr. 1987, pp. 277-301.
16. Noor, Ahmed K.; and Peters, Jeanne M.: Stress and Vibration Analyses of Anisotropic Shells of Revolution. *Int. J. Numer. Methods Eng.*, vol. 26, no. 5, May 1988, pp. 1145-1167.
17. Noor, Ahmed K.; and Tanner, John A.: *Advances in Contact Algorithms and Their Application to Tires*. NASA TP-2781, 1988.
18. *User's Manual -IMSL Math/Library, Version 1.1*. MALB-USM-PERFCT-EN8901-1.1. IMSL, Inc., Jan. 1989.
19. Cline, Alan Kaylor: *Fitpack - A Software Package for Curve and Surface Fitting Employing Splines Under Tension*. Pleasant Valley Software, c.1985.
20. De Boor, Carl: *A Practical Guide to Splines*. Springer-Verlag, c.1978.
21. Reinsch, Christian H.: Smoothing by Spline Functions. *Numer. Math.*, vol. 10, no. 3, 1967, pp. 177-183.
22. Walter, J. D.: Cord Reinforced Rubber. *Mechanics of Pneumatic Tires*, Samuel K. Clark, ed., U.S. Dep. of Transportation, 1981, pp. 123-202.
23. Jones, Robert M.: *Mechanics of Composite Materials*. McGraw-Hill Book Co., c.1975.
24. Cline, A. K.: Scalar- and Planar-Valued Curve Fitting Using Splines Under Tension. *Commun. ACM*, vol. 17, no. 4, Apr. 1974, pp. 218-220.

Table 1. Symmetric and Antisymmetric Tire Parameters With Respect to $\theta = 0$

	Symmetric set	Antisymmetric set
Strain components		
$\{E\}_n$	$\varepsilon_{s,n}, \varepsilon_{\theta,n}, 2\bar{\varepsilon}_{s\theta,n}, \kappa_{s,n},$ $\kappa_{\theta,n}, 2\bar{\kappa}_{s\theta,n}, 2\varepsilon_{s3,n}, 2\bar{\varepsilon}_{\theta3,n}$	$\bar{\varepsilon}_{s,n}, \bar{\varepsilon}_{\theta,n}, 2\varepsilon_{s\theta,n}, \bar{\kappa}_{s,n},$ $\bar{\kappa}_{\theta,n}, 2\kappa_{s\theta,n}, 2\bar{\varepsilon}_{s3,n}, 2\varepsilon_{\theta3,n}$
Stress resultants		
$\{H\}_n$	$N_{s,n}, N_{\theta,n}, \bar{N}_{s\theta,n}, M_{s,n},$ $M_{\theta,n}, \bar{M}_{s\theta,n}, Q_{s,n}, \bar{Q}_{\theta,n}$	$\bar{N}_{s,n}, \bar{N}_{\theta,n}, N_{s\theta,n}, \bar{M}_{s,n},$ $\bar{M}_{\theta,n}, M_{s\theta,n}, \bar{Q}_{s,n}, Q_{\theta,n}$
Generalized displacements		
$\{X\}_n$	$u_n, \bar{v}_n, w_n, \phi_{s,n}, \bar{\phi}_{\theta,n}$	$\bar{u}_n, v_n, \bar{w}_n, \bar{\phi}_{s,n}, \phi_{\theta,n}$

Table 2. Different Types of Coupling in Analysis of Tires With Semianalytic Finite Elements

Response	Material	Governing finite-element equations
Linear	Isotropic or orthotropic	Uncoupled in harmonics Symmetric and antisymmetric variables uncoupled
	Anisotropic	Uncoupled in harmonics Symmetric and antisymmetric variables uncoupled
Nonlinear	Anisotropic	Coupled in harmonics Symmetric and antisymmetric variables coupled

Table 3. Variation of Ply Thickness h_k/h_o [$h_o = 0.7513$ in.]

Ply number (top to bottom)	h_k/h_o for region—						
	I	II	III	IV	V	VI	VII
1 (tread and sidewall)	$h_1 = h - \sum_{k=2}^{16} h_k$						
^a 2	0.0865– .0865	0.0865– .0658	0.0658– .0692	0.0692– .0813	0.0801– .0937	0.0681– .1238	0.0918– .1240
3	.0865– .0865	.0865– .0658	.0658– .0692	.0692– .0813	.0801– .0937	.0681– .1238	.0918– .1240
4	.0865– .0865	.0666– .0506	.0506– .0532	.0692– .0813	.0488– .0571	.0523– .0950	.0652– .0880
5	.0666– .0666	.0666– .0506	.0506– .0532	.0426– .0500	.0488– .0571	.0523– .0950	.0652– .0880
6	.0666– .0666	.0666– .0506	.0506– .0532	.0426– .0500	.0488– .0571	.0523– .0950	^b .2662– .3594
7	.0666– .0666	.0666– .0506	.0506– .0532	.0426– .0500	.0488– .0571	.0523– .0950	.0652– .0880
8	.0666– .0666	.0666– .0506	.0506– .0532	.0426– .0500	.0488– .0571	.0523– .0950	.0652– .0880
9	.0666– .0666	.0666– .0506	.0506– .0532	.0426– .0500	.0488– .0571	.0523– .0950	.0652– .0880
10	.0666– .0666	.0466– .0354	.0354– .0373	.0426– .0500	.0488– .0571	.0523– .0950	.0652– .0880
11	.0466– .0466	.0466– .0354	.0354– .0373	.0346– .0407	.0488– .0571	.0523– .0950	^b .2662– .3594
12	.0466– .0466	.0798– .0798	.0798– .0798	.0346– .0407	.0375– .0439	.0523– .0950	.0652– .0880
13	.0798– .0798	0	0	.0798– .0798	.0375– .0439	.0523– .0950	.0652– .0880
14	0	0	0	0	.0798– .0798	.0366– .0666	.0466– .0629
15	0	0	0	0	0	.0366– .0666	.0466– .0629
16	0	0	0	0	0	.0798– .1464	.1464– .1597

^aSecond layer of region I represents the layer which has the reinforcement (see fig. 2).^bThis represents the thickness of the bead wires.

Table 4. Values of Elastic Constants of Tire Constituents Used in Present Study

Tire constituent	Young's modulus, psi	Shear modulus, psi	Poisson's ratio
Rubber	4.5×10^2	1.51×10^2	0.49
Nylon cord	3.5×10^5	7.00×10^2	.66
Bead ^a	2.9×10^7	1.10×10^7	.30

^aSince the deformations are small in the bead area, it is reasonable to assume that the bead wires are isotropic.

Table 5. Variation of Nylon Cord End Counts in Different Plies Along Meridian

Ply number (top to bottom)	Cord end count, ends per inch for region						
	I	II	III	IV	V	VI	VII
1 tread and sidewall	Rubber	Rubber	Rubber	Rubber	Rubber	Rubber	Rubber
2	16-16	18-14	14-14	14-14	14-14	14-14	14-14
3	18-18	18-14	14-14	14-14	14-14	14-14	14-14
4	18-18	21-20	20-18	18-16	16-16	16-14	14-14
5	23-21	21-20	20-18	18-16	16-16	16-14	14-14
6	23-21	21-20	20-18	18-16	16-16	16-14	Bead
7-9	23-21	21-20	20-18	18-16	16-16	16-14	14-14
10	23-21	29-26	26-25	18-16	16-16	16-14	14-14
11	30-29	29-26	26-25	25-24	16-16	16-14	Bead
12	30-29	Rubber	Rubber	25-24	24-22	16-14	14-14
13	Rubber			Rubber	24-22	16-14	14-14
14				Rubber	Rubber	22-22	22-22
15					22-22	22-22	
16						Rubber	Rubber

Table 6. Variation of Cord Orientation of Individual Plies, θ_k , Along Meridian Region

Ply number (top to bottom)	θ_k , deg, for region—						
	I	II	III	IV	V	VI	VII
1	Rubber	Rubber	Rubber	Rubber	Rubber	Rubber	Rubber
2	$-\tilde{\theta} - 6$	$\tilde{\theta}$	$\tilde{\theta}$	$\tilde{\theta}$	$\tilde{\theta}$	$\tilde{\theta}$	$\tilde{\theta}$
3	$+\tilde{\theta}$	$-\tilde{\theta}$	$-\tilde{\theta}$	$-\tilde{\theta}$	$-\tilde{\theta}$	$-\tilde{\theta}$	$-\tilde{\theta}$
4	$-\tilde{\theta}$	$\tilde{\theta}$	$\tilde{\theta}$	$-\tilde{\theta}$	$-\tilde{\theta}$	$-\tilde{\theta}$	$\tilde{\theta}$
5	$\tilde{\theta}$	$-\tilde{\theta}$	$-\tilde{\theta}$	$\tilde{\theta}$	$\tilde{\theta}$	$\tilde{\theta}$	$-\tilde{\theta}$
6	$-\tilde{\theta}$	$\tilde{\theta}$	$\tilde{\theta}$	$-\tilde{\theta}$	$\tilde{\theta}$	$-\tilde{\theta}$	Bead
7	$\tilde{\theta}$	$-\tilde{\theta}$	$-\tilde{\theta}$	$\tilde{\theta}$	$-\tilde{\theta}$	$\tilde{\theta}$	$-\tilde{\theta}$
8	$-\tilde{\theta}$	$\tilde{\theta}$	$\tilde{\theta}$	$-\tilde{\theta}$	$\tilde{\theta}$	$-\tilde{\theta}$	$\tilde{\theta}$
9	$\tilde{\theta}$	$-\tilde{\theta}$	$-\tilde{\theta}$	$\tilde{\theta}$	$-\tilde{\theta}$	$\tilde{\theta}$	$-\tilde{\theta}$
10	$-\tilde{\theta}$	$\tilde{\theta} + 6$	$\tilde{\theta} + 6$	$-\tilde{\theta}$	$\tilde{\theta}$	$-\tilde{\theta}$	$\tilde{\theta}$
11	$\tilde{\theta} + 6$	$-\tilde{\theta} - 6$	$-\tilde{\theta} - 6$	$\tilde{\theta} + 6$	$-\tilde{\theta}$	$\tilde{\theta}$	Bead
12	$-\tilde{\theta} - 6$	Rubber	Rubber	$-\tilde{\theta} - 6$	$\tilde{\theta} + 6$	$\tilde{\theta}$	$\tilde{\theta}$
13	Rubber			Rubber	$-\tilde{\theta} - 6$	$-\tilde{\theta}$	$-\tilde{\theta}$
14					Rubber	$\tilde{\theta} + 6$	$\tilde{\theta} + 6$
15						$-\tilde{\theta} - 6$	$-\tilde{\theta} - 6$
16						Rubber	Rubber

Table 7. Maximum Absolute Values of Normal Displacement Components w_n
[Tire shown in fig. 2; $p_{o,\max} = 445.3$ psi; $h_o = 0.7513$ in.; $E_{T_o} = 1160.3$ psi]

Fourier harmonic, n	$w_n E_{T_o} / (p_{o,\max} h_o)$	Fourier harmonic, n	$w_n E_{T_o} / (p_{o,\max} h_o)$
1	18.08	6	1.095
2	11.41	7	.3122
3	7.110	8	1.134
4	4.841	9	1.424
5	2.906	10	1.313

Table 8. Maximum Absolute Values of In-Plane Displacements and Rotation Components
[Tire shown in fig. 2; $p_{o,\max} = 445.3$ psi; $h_o = 0.7513$ in.; $E_{T_o} = 1160.3$ psi]

Displacements and rotations	Fourier harmonic		
	$n = 1$	$n = 5$	$n = 10$
$u_n E_{T_o} / (p_{o,\max} h_o)$	7.584	0.3266	1.229×10^{-1}
$v_n E_{T_o} / (p_{o,\max} h_o)$.04162	.01139	3.773×10^{-3}
$\phi_{s,n} E_{T_o} / p_{o,\max}$	3.602	.4840	1.304×10^{-1}
$\phi_{\theta,n} E_{T_o} / p_{o,\max}$.1805	.01271	6.982×10^{-3}

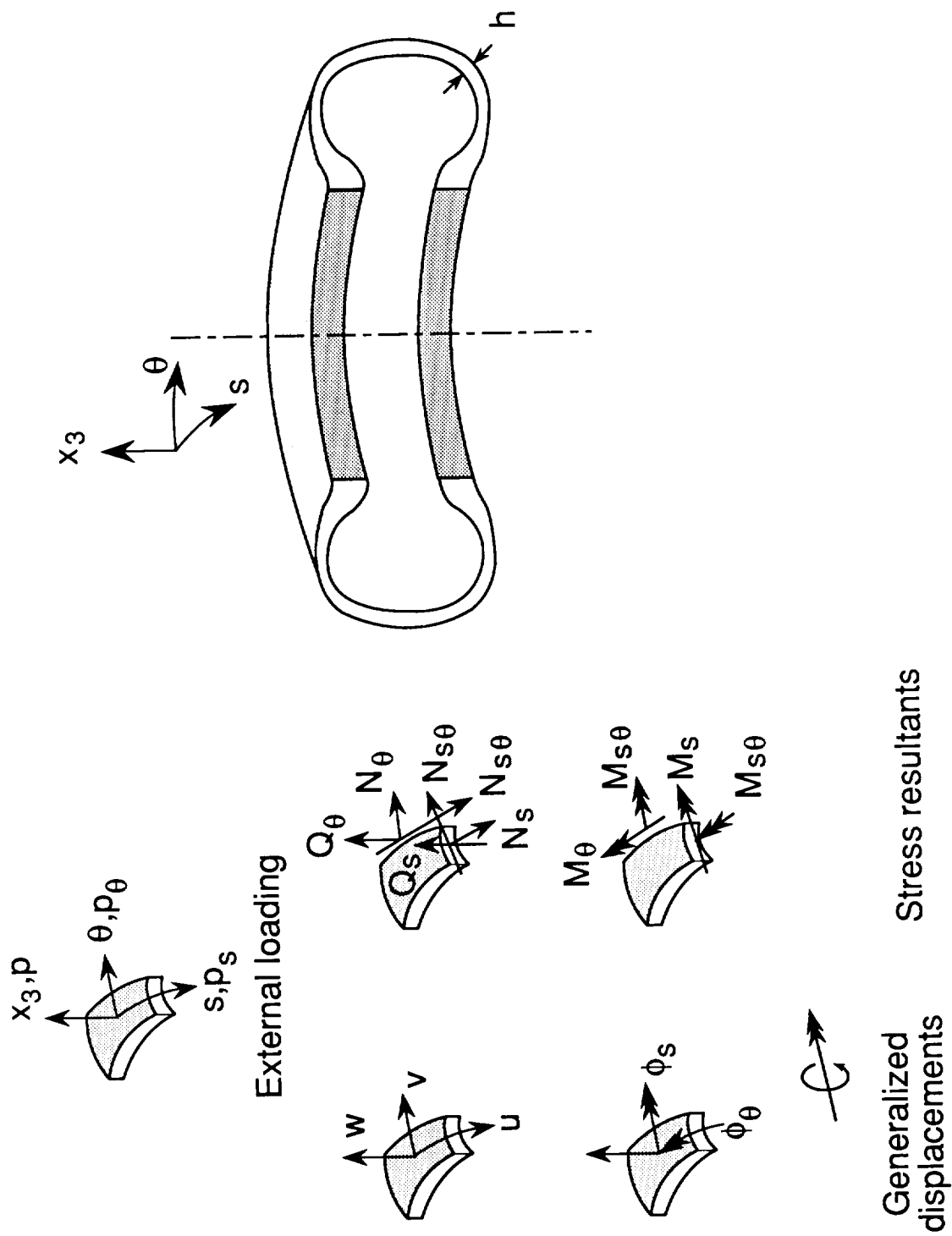


Figure 1. Two-dimensional shell model of tire and sign convention for external loading, generalized displacements, and stress resultants.

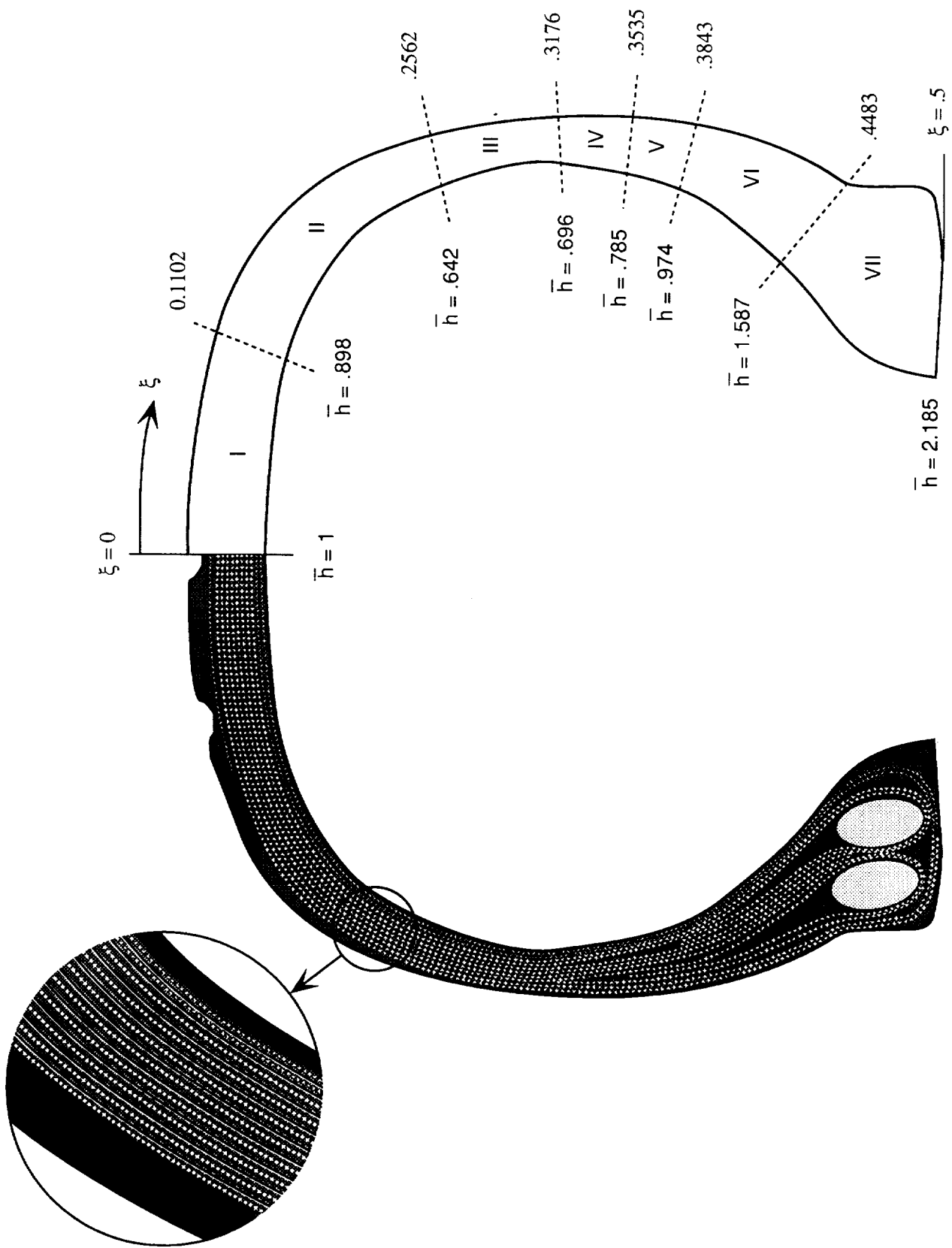


Figure 2. Tire cross section and thickness variation for Space Shuttle orbiter nose-gear tire used in present study. $\bar{h} = h/h_o$.

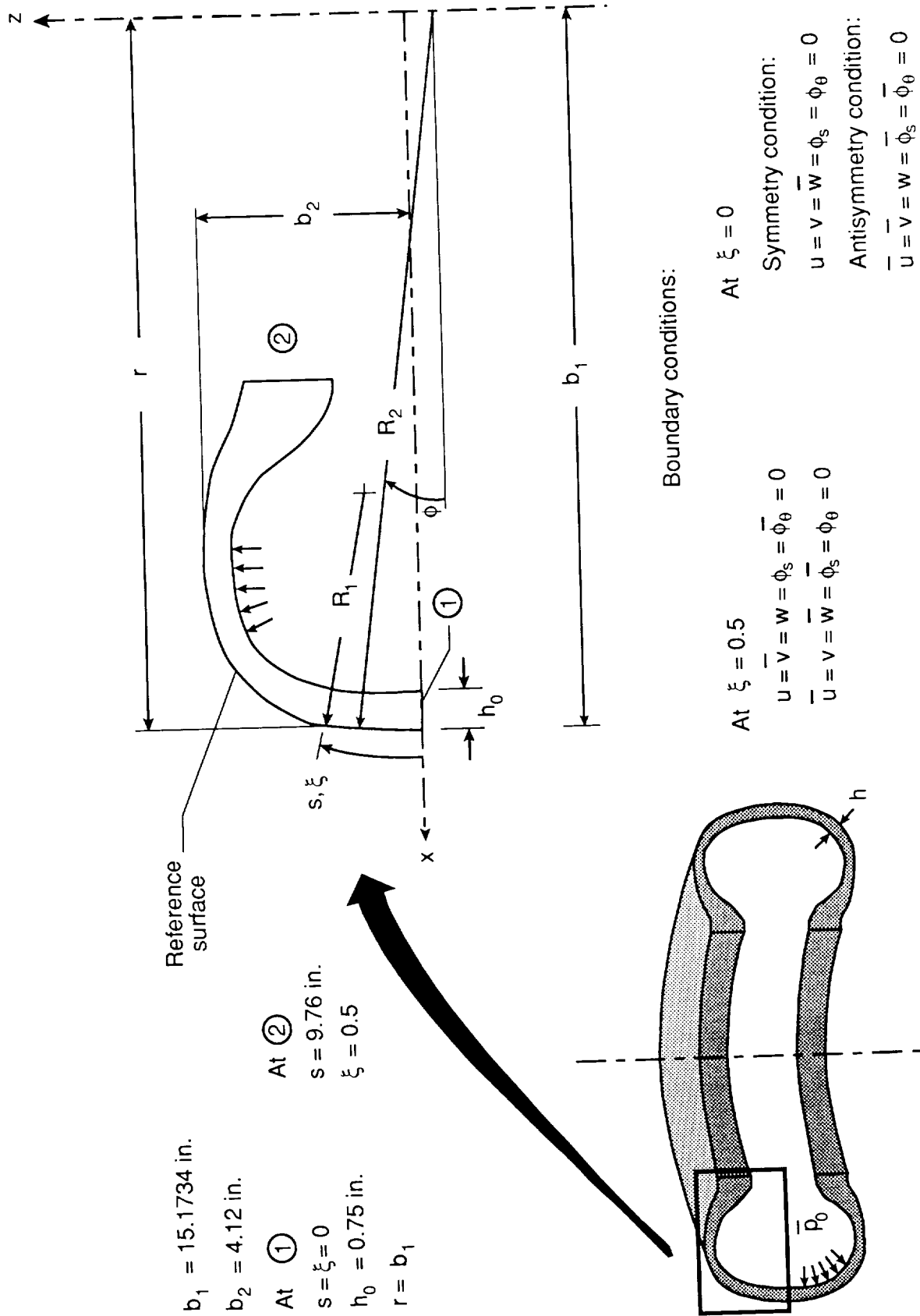
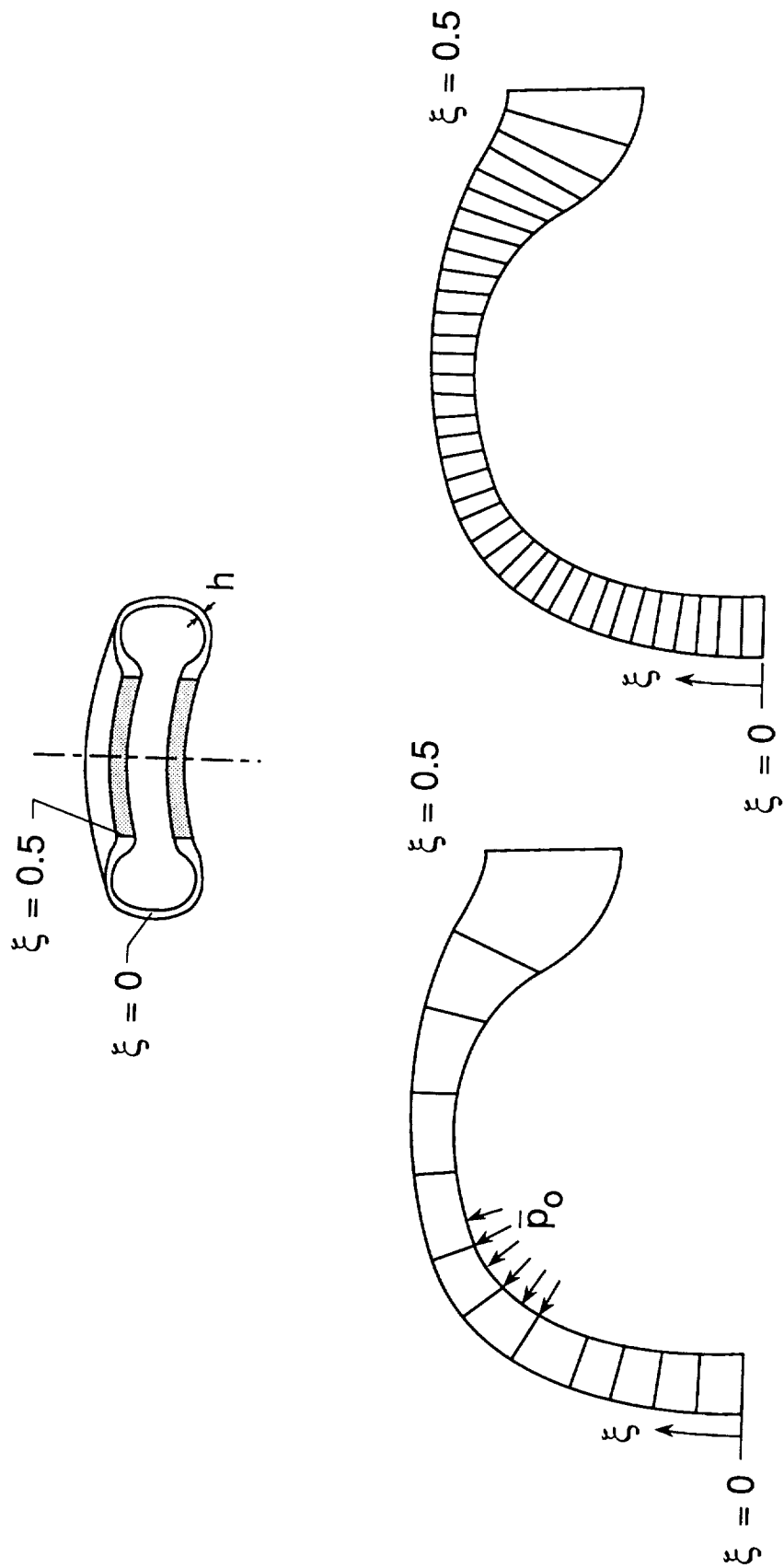


Figure 3. Characteristics of Space Shuttle orbiter nose-gear tire used in present study. $\bar{h} = h/h_0$.



(a) Inflation pressure.

(b) Localized normal loading on outer surfaces.

Figure 4. Finite-element models used in present study.

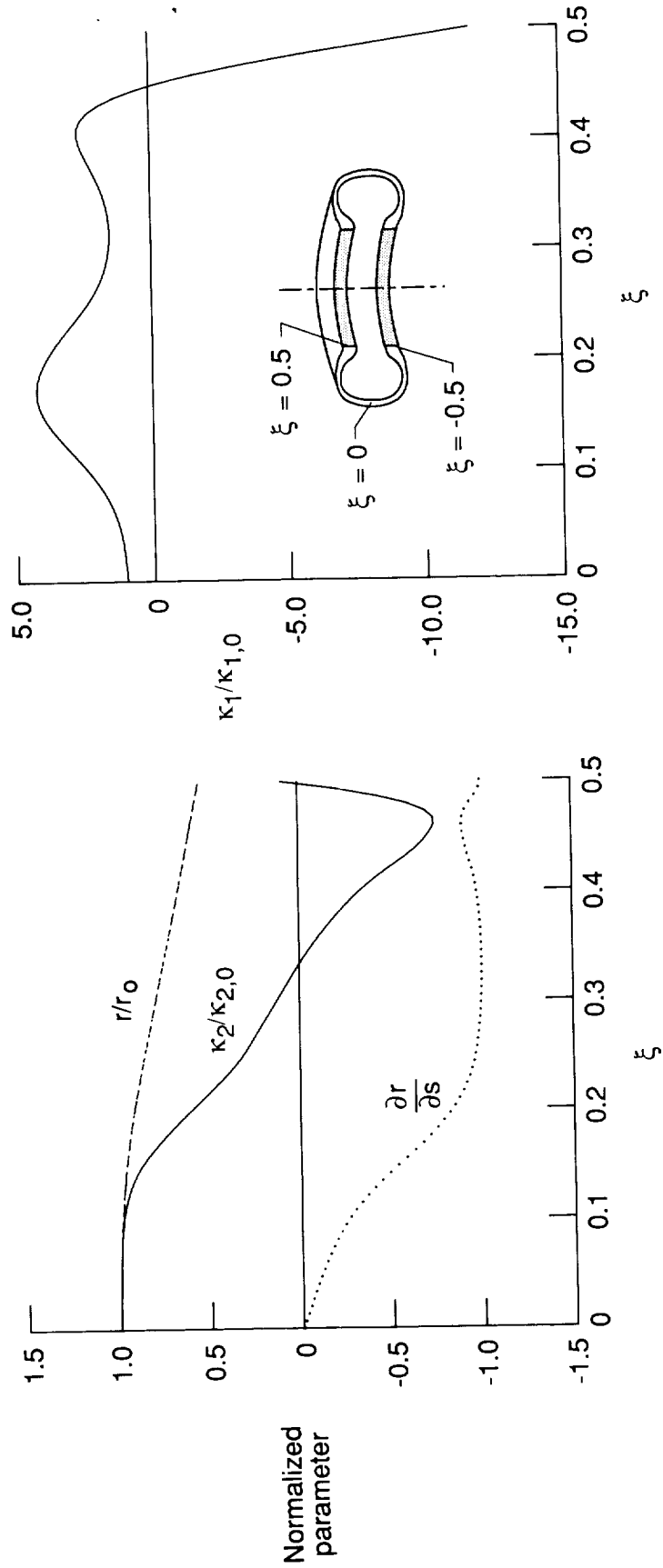
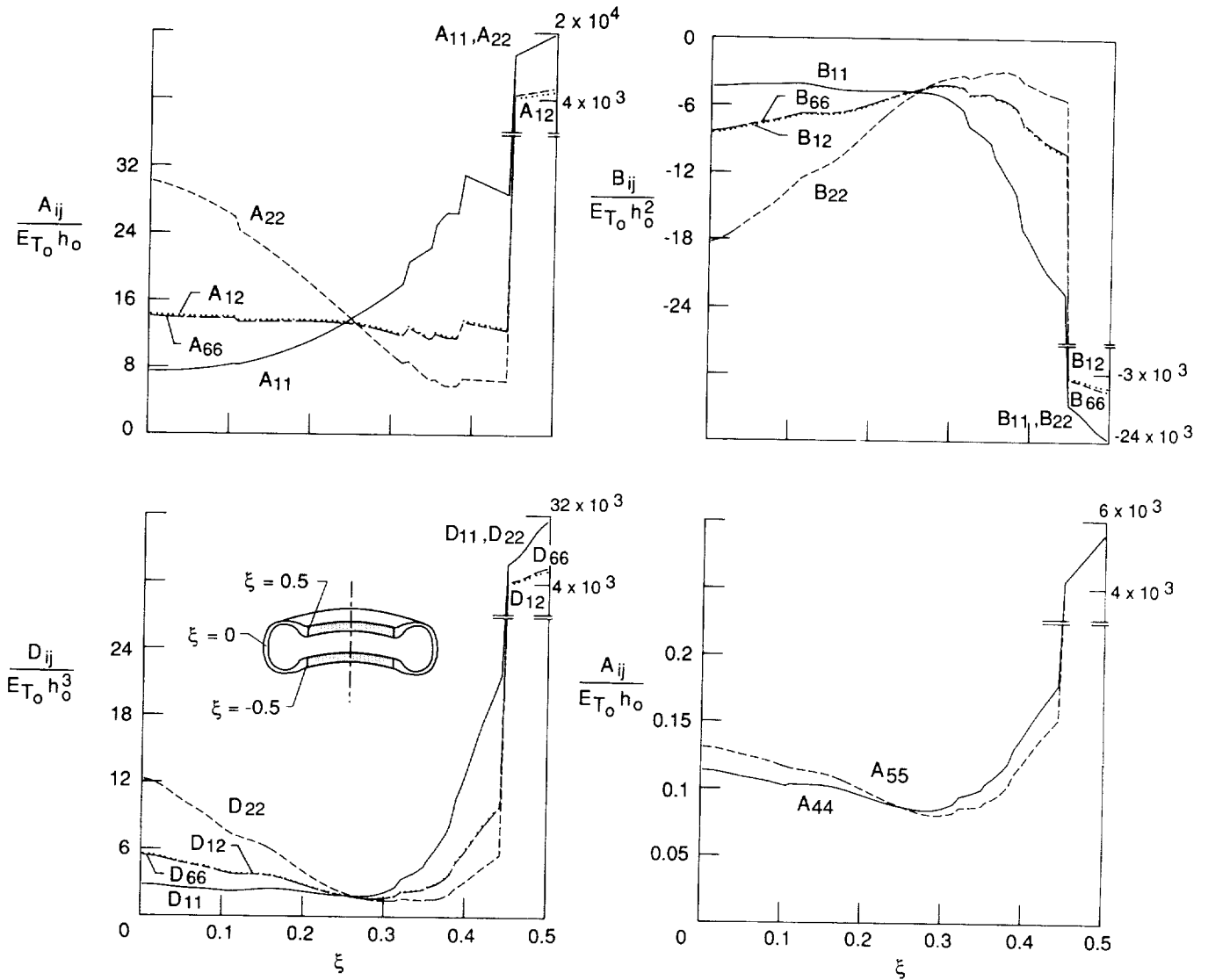


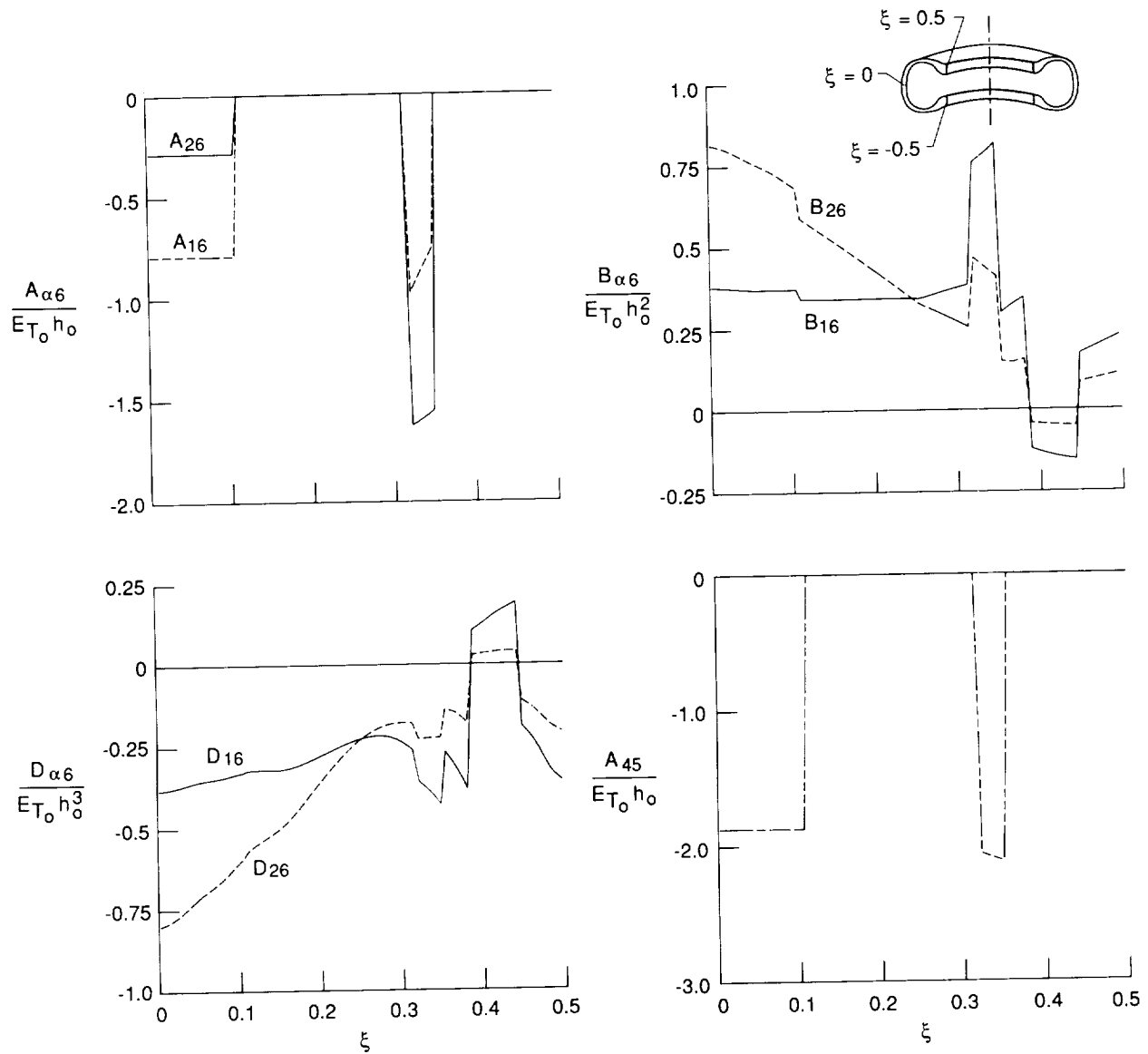
Figure 5. Meridional variation of geometric parameters of two-dimensional shell model of Space Shuttle orbiter nose-gear tire. Reference surface chosen to be outer surface. $\tau_o = 15.1737$ in.; $\kappa_{2,0} = 0.0659$ in⁻¹; $\kappa_{1,0} = 0.1091$ in⁻¹.



(a) Stiffness coefficients associated with uncoupled (orthotropic) response.

Figure 6. Meridional variation of stiffness coefficients of two-dimensional shell model of Space Shuttle orbiter nose-gear tire. $E_{T_o} = 1160.3$ psi.

ORIGINAL PAGE IS
OF POOR QUALITY



(b) Coupling (nonorthotropic) stiffness coefficients. $\alpha = 1, 2$.

Figure 6. Concluded.

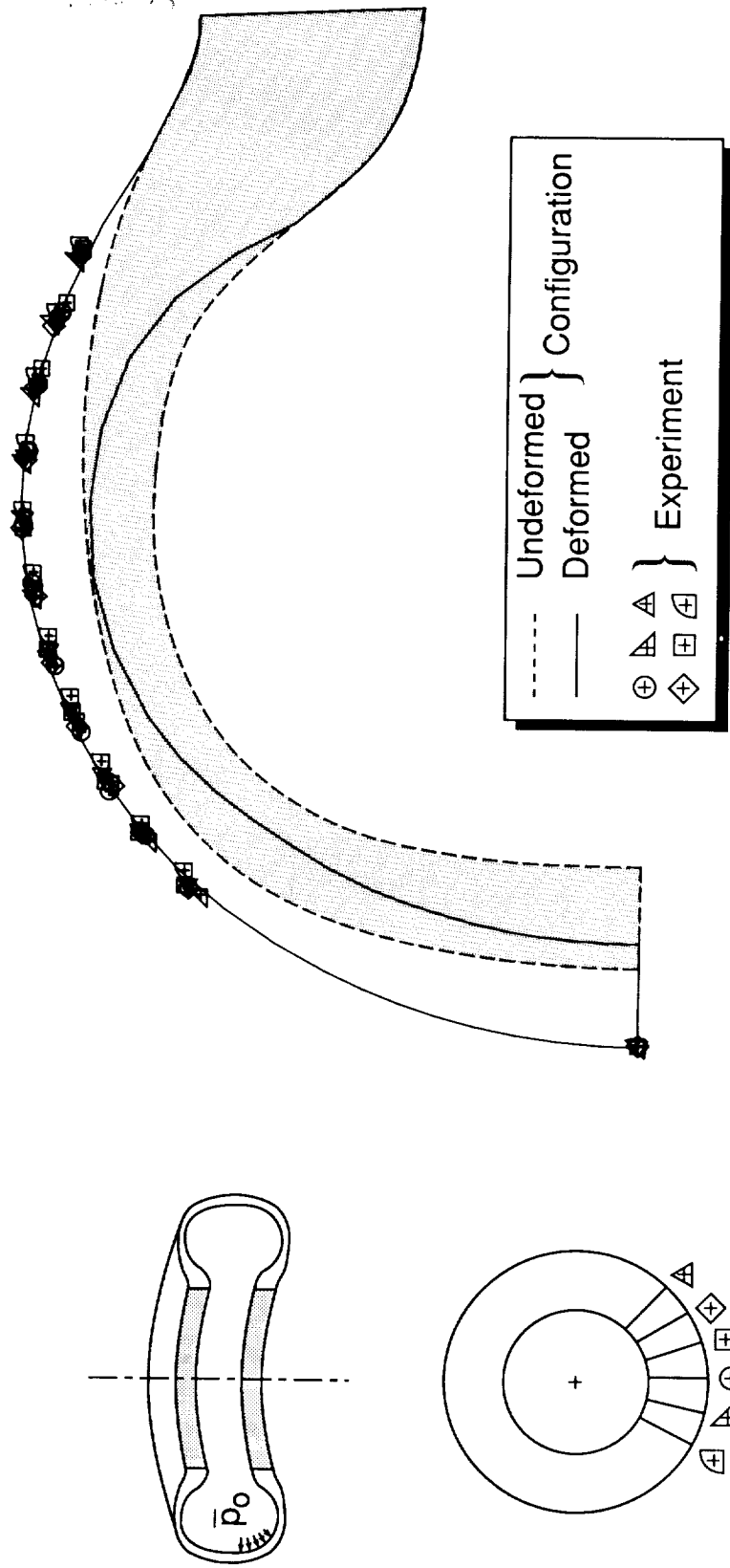


Figure 7. Experimental and predicted two-dimensional shell model of Space Shuttle orbiter nose-gear tire.
 $\bar{p}_0 = 320$ psi.

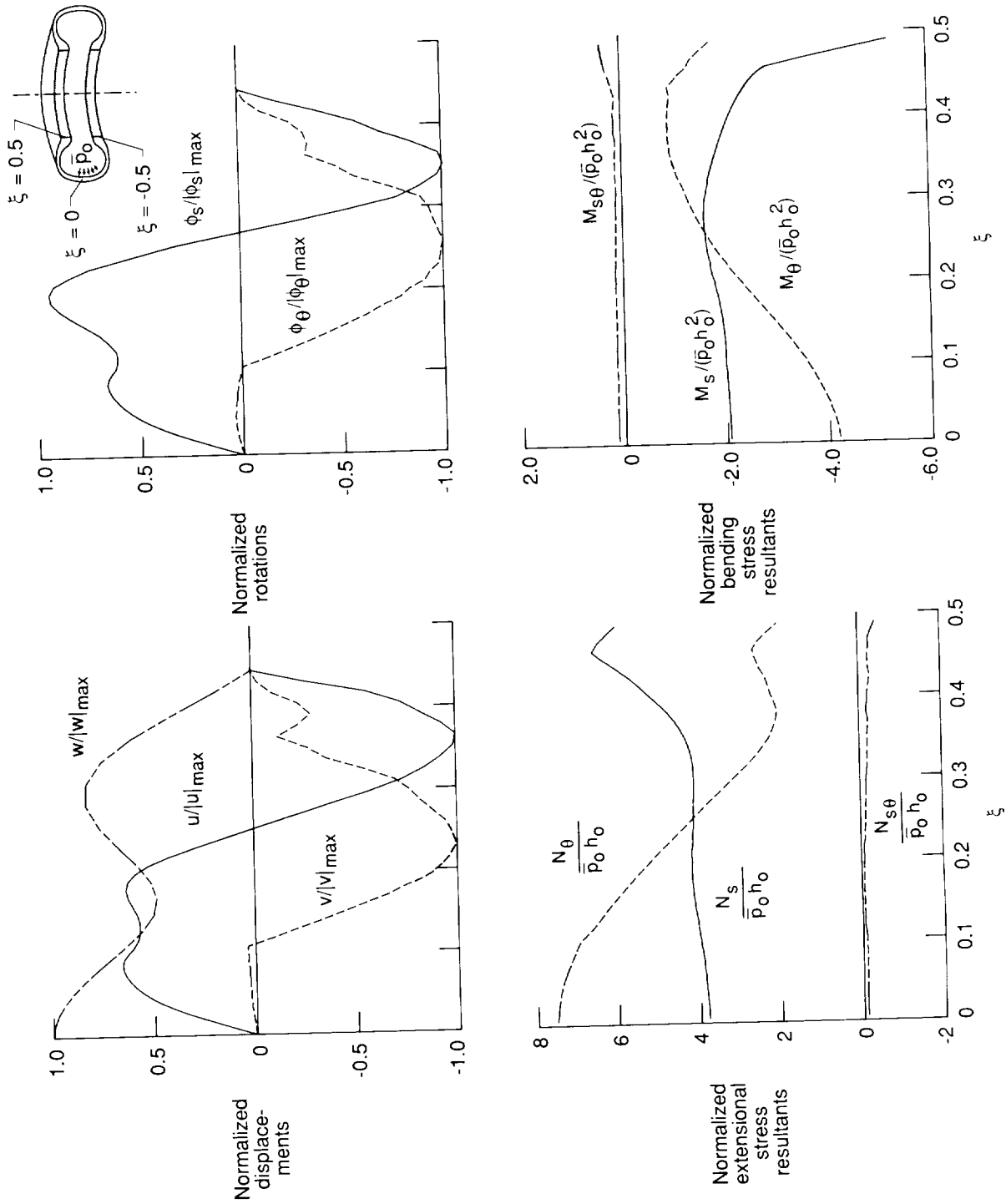


Figure 8. Meridional variation of generalized displacements and stress resultants produced by inflation pressure using two-dimensional shell model of Space Shuttle orbiter nose-gear tire. $|u|_{\max} = 0.1440$ in.; $|v|_{\max} = 0.02365$ in.; $|w|_{\max} = 0.5689$ in.; $|\phi_s|_{\max} = 0.309$; $|\phi_\theta|_{\max} = 6.509 \times 10^{-2}$.

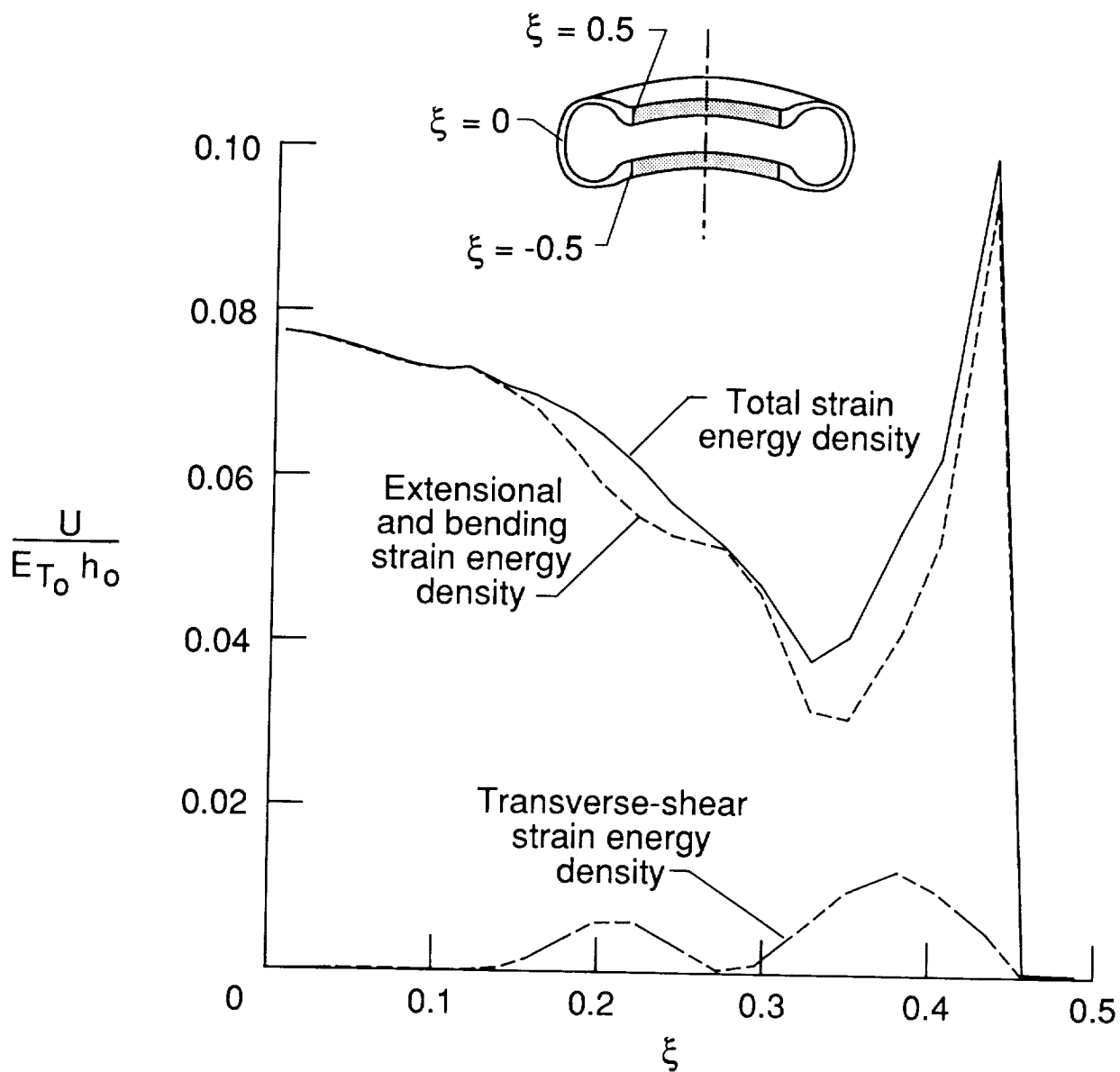


Figure 9. Meridional variation of strain energy densities produced by inflation pressure using two-dimensional shell model of Space Shuttle orbiter nose-gear tire.

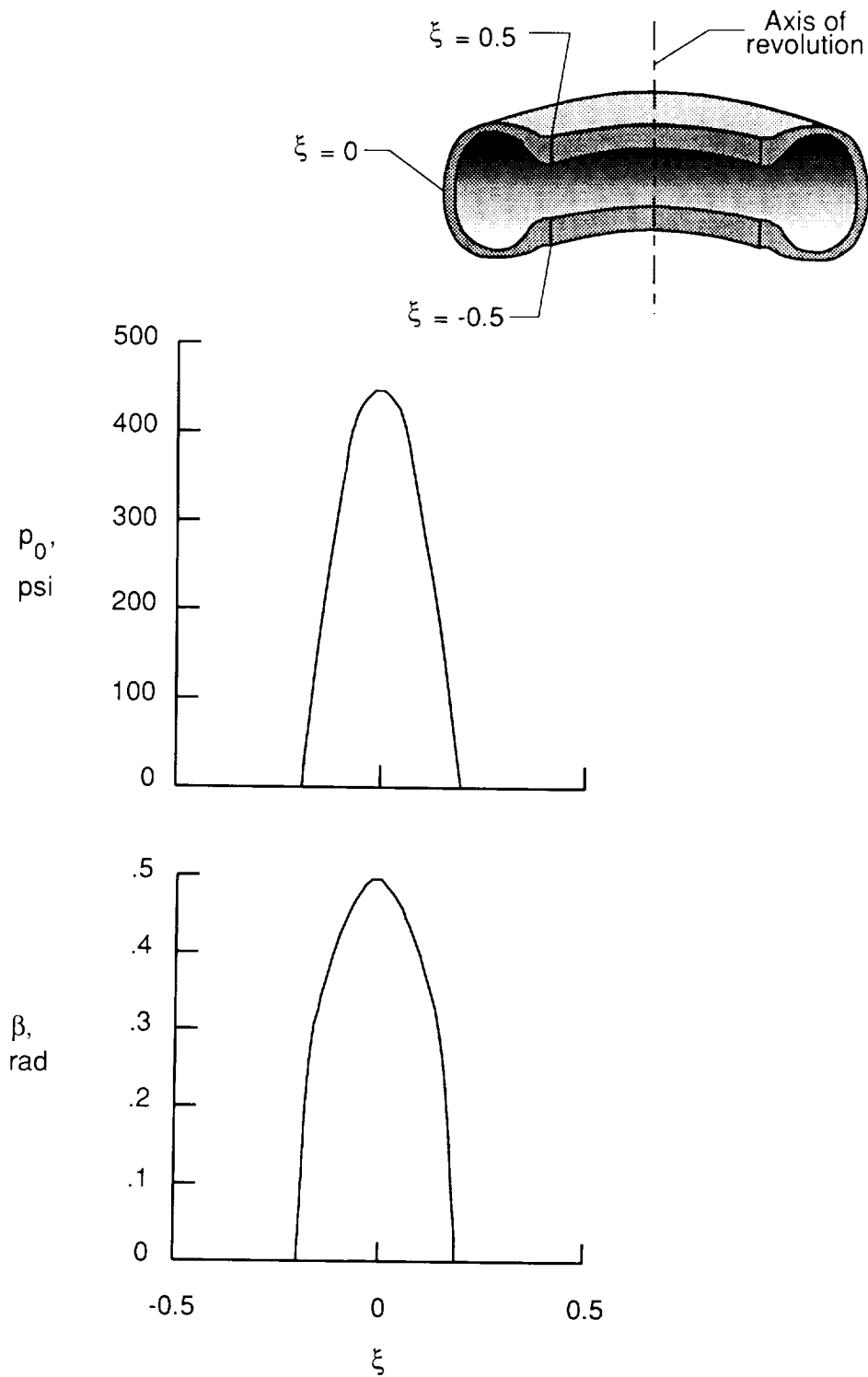


Figure 10. Variation of contact pressure and contact angle in meridional direction. $p_{o,\max} = 445.266$ psi; $\beta_{\max} = 0.49375$ rad.

ORIGINAL PAGE IS
OF POOR QUALITY

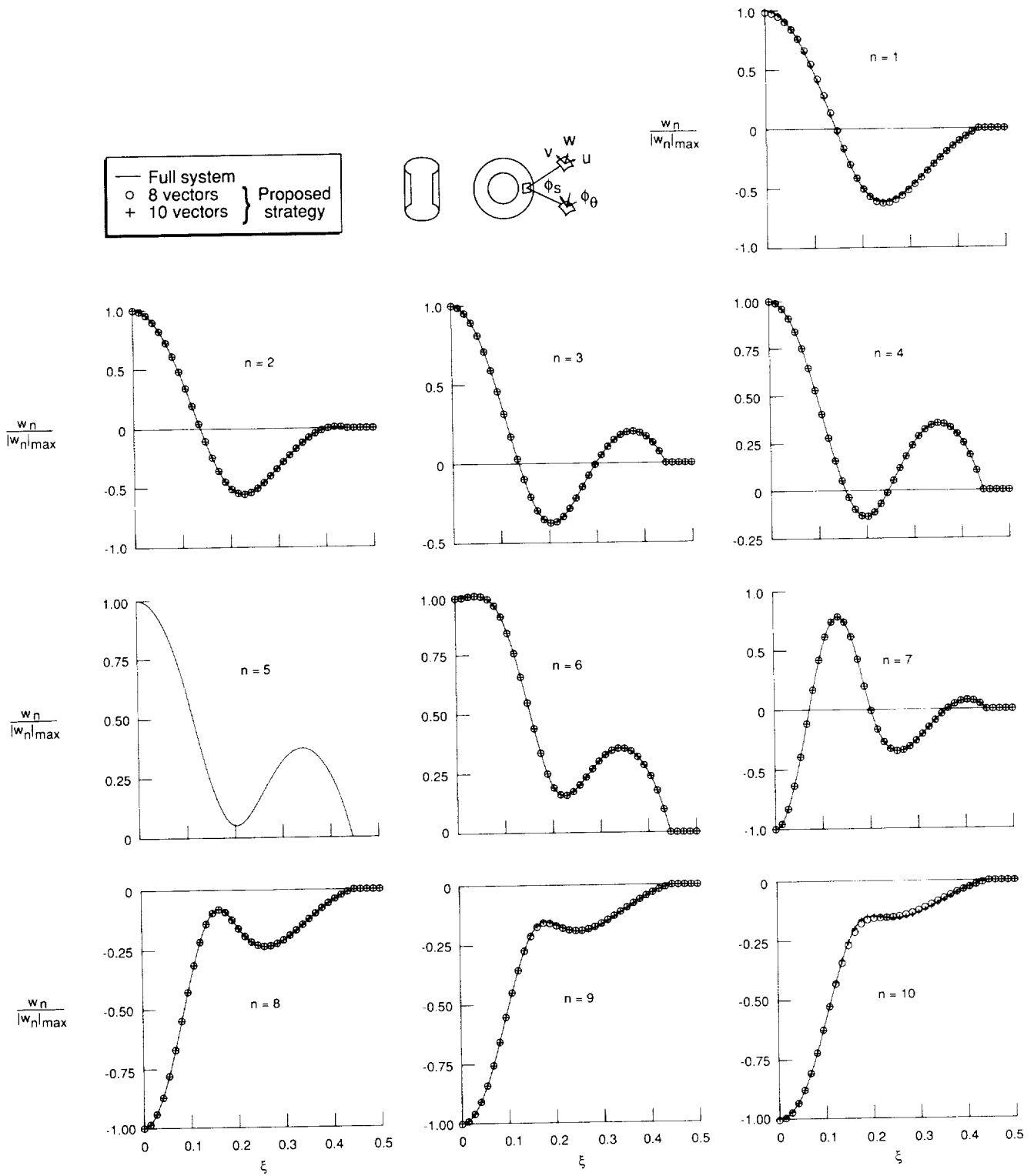


Figure 11. Accuracy of normal displacements w_n obtained with proposed procedure using two-dimensional shell model of Space Shuttle orbiter nose-gear tire.

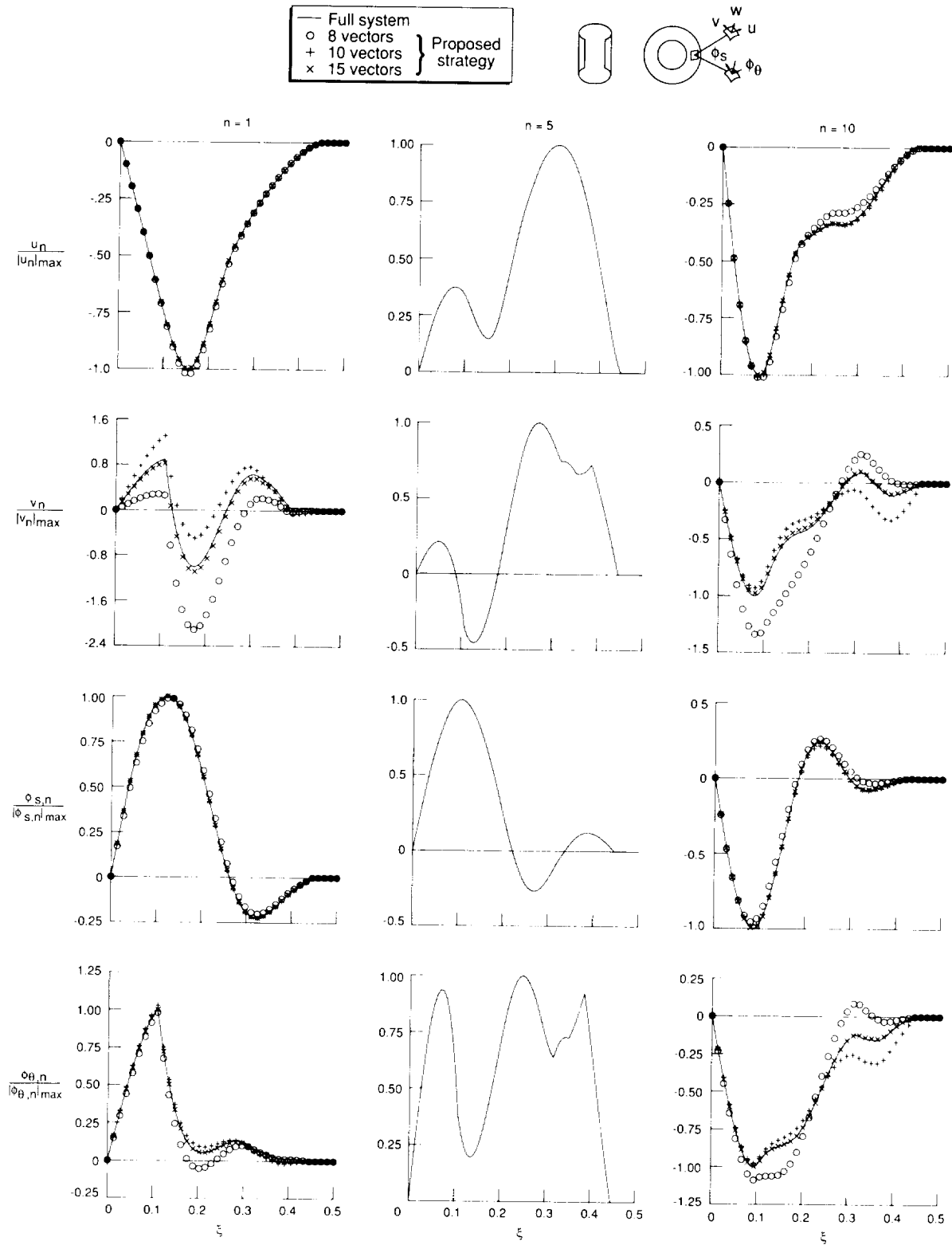


Figure 12. Accuracy of in-plane displacements and rotation components obtained with proposed procedure using two-dimensional shell model of Space Shuttle orbiter nose-gear tire.



Report Documentation Page

1. Report No. NASA TP-2977	2. Government Accession No.	3. Recipient's Catalog No.	
4. Title and Subtitle Modeling and Analysis of the Space Shuttle Nose-Gear Tire With Semianalytic Finite Elements		5. Report Date April 1990	
		6. Performing Organization Code	
7. Author(s) Kyun O. Kim, Ahmed K. Noor, and John A. Tanner		8. Performing Organization Report No. L-16639	
		10. Work Unit No. 505-63-41-02	
9. Performing Organization Name and Address NASA Langley Research Center Hampton, VA 23665-5225		11. Contract or Grant No.	
		13. Type of Report and Period Covered Technical Paper	
12. Sponsoring Agency Name and Address National Aeronautics and Space Administration Washington, DC 20546-0001		14. Sponsoring Agency Code	
15. Supplementary Notes Kyun O. Kim and Ahmed K. Noor: The George Washington University, Joint Institute for Advancement of Flight Sciences, Langley Research Center, Hampton, Virginia. John A. Tanner: Langley Research Center, Hampton, Virginia.			
16. Abstract A computational procedure is presented for the geometrically nonlinear analysis of aircraft tires. The Space Shuttle orbiter nose-gear tire was modeled through use of a two-dimensional laminated anisotropic shell theory with the effects of variation in material and geometric parameters included. The four key elements of the procedure are (1) semianalytic finite elements in which the shell variables are represented by Fourier series in the circumferential direction and piecewise polynomials in the meridional direction; (2) a mixed formulation with the fundamental unknowns consisting of strain parameters, stress-resultant parameters, and generalized displacements; (3) multilevel operator splitting to effect successive simplifications and to uncouple the equations associated with different Fourier harmonics; and (4) multilevel iterative procedures and reduction techniques to generate the response of the shell. Numerical results of the Space Shuttle orbiter nose-gear tire model are compared with experimental measurements of the tire subjected to inflation loading.			
17. Key Words (Suggested by Authors(s)) Shuttle nose-gear tire Tire modeling Semianalytic finite elements Mixed formulation Reduction techniques Operator splitting		18. Distribution Statement Unclassified— Unlimited Subject Category 39	
19. Security Classif. (of this report) Unclassified	20. Security Classif. (of this page) Unclassified	21. No. of Pages 34	22. Price A03